UNIVERSITÀ DEGLI STUDI DI PALERMO

Dottorato di Ricerca in "Scienze Fisiche"

Dipartimento di Fisica e Chimica (DiFC)

Settore Astronomia e Astrofisica (FIS/05)

Accretion disk coronae of Intermediate Polar Cataclysmic Variables: 3D MagnetoHydroDynamic modeling and thermal X-ray emission

PhD candidate:

Enrico Barbera

Coordinator:

Prof. Gioacchino Massimo Palma

Tutor:

Prof. Giovanni Peres

CICLO XXIX

2017

Contents

Abstract

Intermediate Polar Cataclysmic Variables (*IPCVs*), also known as *DQ Her* stars after their prototype, are cataclysmic variable stars characterized by the presence of an accreting, magnetic, rapidly rotating white dwarf surrounded by an accretion disk magnetically truncated by the inner magnetosphere of the star. These objects exhibit a magnetic field of the order of few MG, able to disrupt the inner part of the disk but not strong enough to inhibit the formation of a disk. These stars show a strong X-ray emission with a stochastic pulsation that in some cases arise in the inner part of the disk. However, the observations of the X-ray luminosity for these objects do not match the expected value: *IPCVs* appear in general to be underluminous in X-ray than expected for an accreting white dwarf. Nevertheless, accretion processes have often been successfully taken into account in order to explain the observed X-ray emission from *IPCVs*, although the observed features suggest that accretion phenomena occurring in these objects could be not the only process behind the X-ray emission.

The main purposes of the present thesis are the following: the primary aim is to investigate the formation of an extended corona above the accretion disk, due to an intense flaring activity occurring on the disk surface; another objective is investigate its effects on the disk, on the accretion and on the stellar magnetosphere; the last, but not less important, intent is to assess the contribution of this coronal activity to the observed thermal X-ray fluxes.

To this end we have developed a 3D magnetohydrodynamic (MHD) model describing an *IPCV* system. The model takes into account gravity, viscosity, thermal conduction, radiative losses and coronal heating. In order to carry out a parameter space exploration, several system conditions have been considered, with different magnetic field intensity and disk density. From the results of the evolution of the model, we have synthesized the thermal X-ray emission.

The simulations actually show the formation of an extended corona, linking disk and star. The coronal activity is capable of strongly influencing the disk configuration and possibly its stability, effectively deforming the magnetic field lines. Hot plasma evaporation phenomena occur in the layer immediately above the disk. Furthermore, the flaring activity

give rise to a conspicuous thermal X-ray emission in both the $[0.1 - 2.0]$ keV and the $[2.0 - 10]$ keV X-ray bands.

In the light of our findings, it is possible to conclude that an intense coronal activity occurring on the disk surface of an $IPCV$ can affect significantly the structure of the disk and the magnitude of this effect appears noticeably dependent on the density of the disk and the magnetic field of the central object. Moreover, the synthesis of the thermal X-ray fluxes shows that this flaring activity may contribute to the observed flickering thermal X-ray emission.

Chapter 1

Introduction

1.1 Scope of the thesis

Star-disk systems have a key-role in astrophysics due to mass, momentum and energy transport from disk to the star and to the circumstellar medium. Moreover, one of the key elements making these object a very interesting subject of research is that they actually seems to be ubiquitous and they exist in several star evolution phases, from young stellar object (*CTTS - Classical T-Tauri stars*) up to the ultimate remnants of a star (e.g. *LMXB - Low Mass X-Ray Binaries*, *IPCV - Intermediate Polars Cataclysmic Variables*) albeit with very different physical conditions. Furthermore, this kind of star systems, due to their complex structure, exhibit several significant features: for instance, they are characterized by accretion processes, may show a remarkable X-ray emission and are site of several phenomena able to profoundly influence the whole system. In fact, one of the subjects of this thesis is the possible contribution to the global X-ray emission due to a corona of the accretion disk, mostly due to a continuous chain of flaring events, a scenario already suggested in literature (Galeev et al., 1979). The flares are due to magnetic reconnections of magnetic field permeating the disk and continuously wound and stretched by the disk's differential rotation. Flares are events commonly observed on the surface of the Sun, releasing significant amount of energy up to 10^{32} *erg*. There is a general consensus on their origin as an energy release triggered by magnetic reconnection events. Much more energetic flares have been observed on main sequence stars and *CTTS*; some flares occur on the stellar surface but others are quite likely occurring on the disk or in the magnetic loops interconnecting the star and the disk (Favata et al., 2005). Therefore, it is arguable that flares may occur on the accretion disk around some compact objects as well, where conditions of the plasma are analogous to the ones found in the disk of *CTTS*.

In the present thesis we want to explore the various effects of a flaring activity on the surface of the accretion disk of a compact object through magnetohydrodynamic (MHD)

simulations. In order to carry on this investigation, we chose to adopt and tune a model of a class of objects whose features could be modelled without having to cope with very extreme and hard to handle physical conditions and, at the same time, shared many features with both very extreme and with more manageable star-disk systems, thus granting the perspective of safely extending our model: *Intermediate Polar Cataclysmic Variables* (*IPCV*s or *DQ Her*). *IPCV*s is a subclass of the wider *Cataclysmic Variables* class (*CV*s) and represent a good prototype of compact object with accretion disk for several reasons. They combine the features of a weakly magnetized object in the external region of the disk and the ones of a strongly magnetized object in its inner region, where the magnetosphere dominates the accretion. They share several similarities with *CTTS* and similar objects, so the computational model already developed for *CTTS* by Orlando et al. (2011) can be adapted and appropriately scaled. Moreover, they may host flares more energetic than those on the Sun, due to their intense magnetic field.

In the following Section 1.2 we briefly review the main features of *CV*s, focusing on *IPCV*s and stressing the similarities and differences with other subclasses of *CV*s; in the Section 1.3 we describe the main issues and the approach adopted to address them.

1.2 Intermediate Polars and other Cataclysmic Variables

Cataclysmic Variables (CVs) show irregular and large variations in brightness, followed by a quiescent state. This behaviour, at first blush, seems to follow no regular pattern. Initially they have been named after the latin word *Nova*, since this kind of phenomena appeared as new stars in the sky, due to the fact that some of these stars are visible to the naked eye during their outbursts and invisible when quiescent.

As observational data were collected it became clear that these objects were regular binary systems changing in brightness for some reason. Then, Cataclysmic Variables were subdivided into three major groups on the basis of the optical outburst properties and their variability: *Classical Novae (CN)* showing only one significant change in brightness yet observed (with an absolute magnitude variation of 10-11 mag); *Recurrent Novae (RN)* and *Dwarf Novae (DN)* with a regular but smaller variability (respectively of 7-8 mag and 2-3 mag). Actually, a fourth group may be defined by *Nova-like objects (NL)*, stellar objects known to show small and frequent fluctuation in brightness without significant explosions. This feature of *NL* objecs is known as *flickering* and is accountable for variations of the order of tenth of magnitude, lasting seconds or minutes, and fundamentally without periodic behaviour. This phenomenon is observable even in the other types of *CVs* during quiescent phase. So, *NLs* could be *Novae* in stasis with not yet observed eruptions.

Every star in these classes shows common features with the others and peculiarities that

makes them unique. So, it's hard to recognize in the stellar objects just roughly depicted a common scheme lying beneath. Nevertheless, a binary interacting star system is the common basis of all these objects. Both stars are already in the final phase of their lives; the primary star, the most massive one, has evolved faster and it has collapsed becoming a white dwarf (*WD*). In contrast with the compact and hot primary star, the secondary star is a less massive former main-sequence companion, less evolved, less dense and colder. The companion star's external layers fill the *Roche lobe*[1] and material from the secondary star may fall onto the *WD* swirling around this one through a thin mass transfer stream. Fig. 1.1 and 1.2 depict the main elements describing the *CV* stars.

In order to fully understand the difference between various classes of *CVs*, we have to define some important physical quantities involved in their dynamics. In the next section these quantities will allow us to introduce a more specific classification of these object based on the magneto-gravitational interaction between the white dwarf and the circumstellar environment. First, the Alfvén radius (R_A) is the distance from a magnetized star where the magnetic pressure equals the plasma pressure (plus possible ram pressure). In other words, it defines the distance where the β parameter of plasma is equal to unity:

$$\beta = 8\pi \frac{p + \rho v^2}{B^2} = 1. \tag{1.1}$$

In systems where an accretion disk is involved it may be coincident with disk's truncation radius R_d, i.e. the inner end of the disk. Another key parameter is the circularization radius (R_{circ}); this parameter determines the external extension of a accretion disk and it is defined as the radius where angular momentum of material orbiting the *WD* matches the angular momentum of material passing through the lagrangian point between the *Roche lobes* (Hellier, 2007).

$$\omega_{circ} R_{circ}^2 = \omega_{orb} R_{L_1}^2 \tag{1.2}$$

where ω_{orb} is the orbital velocity of the binary system while ω_{circ} is the keplerian angular velocity at the external boundary of the disk $\omega(R_{circ}) = \sqrt{M_{wd} G / R_{circ}^3}$.

1.2.1   Nova-like objects subclass

The most suitable approach to the study of *CVs* from a physical point of view is to consider them as rotating compact object interacting with the surrounding environment through

---

[1]*Roche lobes* define gravitational equipotential surfaces around the binary system.
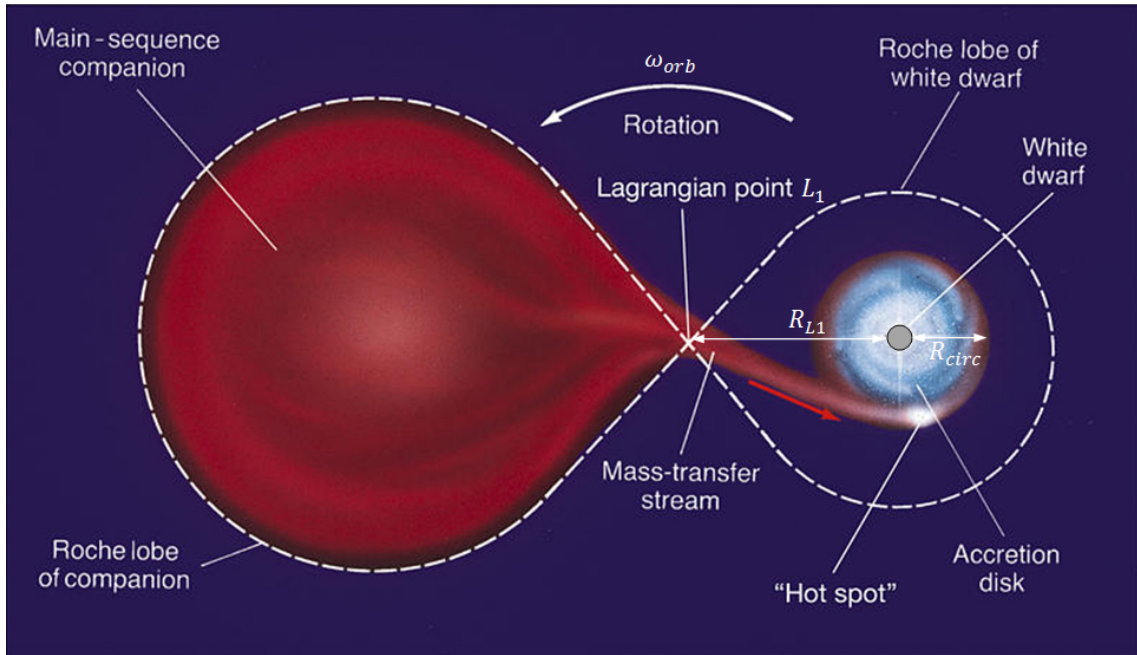
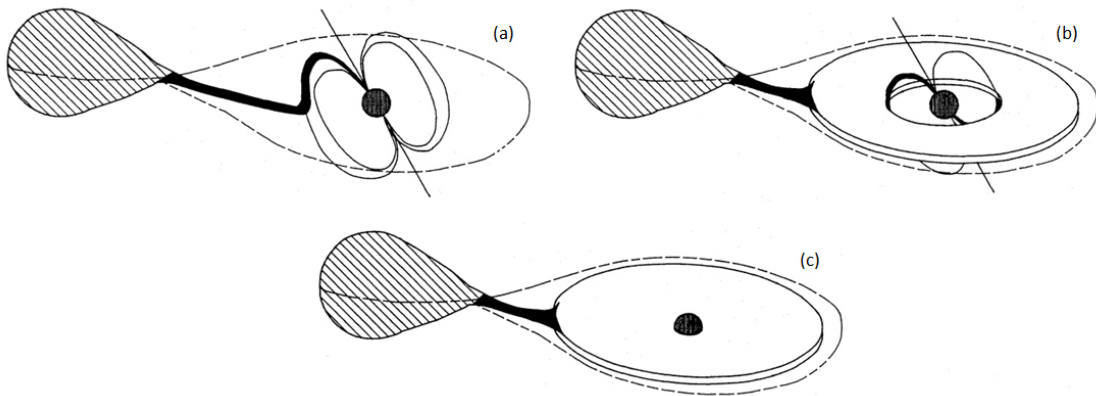**Figure 1.1:** Main elements used to represent a *CV* system.

Figure 1.2: Schematic diagram of accretion process in *CV*s. (a) An *AM Her* star without accretion disk, the accreting material impacts directly on the surface of the white dwarf, flowing through the magnetosphere along field lines. (b) A *DQ Her* star with the accretion disk disrupted at the magnetospheric boundary. (c) A *Non-magnetic CV* with no disruption of the accretion disk (Norton, 1993).

magnetic field and gravity (Giovannelli et al., 2012). As a matter of fact, the magnetic and gravitational forces have a key role in the phenomena occurring in this kind of object, defining an alternative classification of *CVs* and, in particular of the *NL* objects. Indeed, the class of *NL* objects may be divided in two sub-classes: the *AM Her* stars and the *DQ Her* stars, named after their respective star prototypes (Fig. 1.2). The major feature common to these sub-classes of *CVs* is a *WD* with a magnetic field strong enough to dominate all accretion phenomena. Emphasising the paramount importance of magnetic
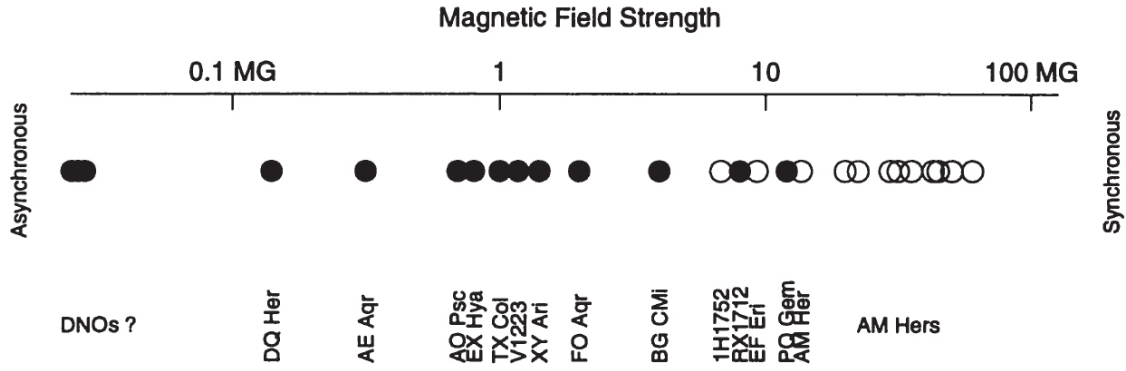
Figure 1.3: Scale of magnetic field strength of *Magnetized Cataclysmic Variables* (*MCV*s) over many order of magnitude from the lowest on the left to the strongest to the right: *PCVs* (open circles) and *IPCVs* (filled circles) form an overlapping continuum (Dhillon, 1996; Seward & Charles, 2010).

field in phenomena occurring in this kind of stellar objects, *AM Her* and *DQ Her* stars took the names of *Polars Cataclysmic Variables* (*PCVs*) and *Intermediate Polars Cataclysmic Variables* (*PCVs*), respectively. In fact, depending on the magnetic field intensity of the *WD*, the accretion of matter from the secondary star onto the primary can occur in different ways. Fig. 1.3 shows the distribution of magnetic field intensity of *Intermediate Polar*s and *Polars*. Hereafter we briefly summarize the main feature of these class of *CV*s in order of increasing magnetic field intensity.

- *PCV*s or *AM Her* stars

  In these objects, also known as *Polar Cataclysmic Variables* (*PCVs*), the accretion process takes place via a direct magnetic channelling through the magnetic poles. This behaviour arises because magnetic field of the *WD* is strong enough ($\sim 10-200MG$) to make the magnetosphere radius (or Alfven radius R_A) greater than the circularization radius (R_{circ}), therefore no accretion disc is formed and the accretion is fully governed by the magnetic field. As shown in Fig. 1.2a, the accretion originates in a stream from the secondary star through the inner lagrangian point (L_1), then it is canalized by the magnetic field along the field lines and poured directly onto the surface of the *WD*. In Cataclysmic Variables with a highly magnetic white dwarf (exceeding $30MG$), the *WD* is usually phase-locked to the orbit and its rotation is synchronized with the binary orbital period (a few hours typically) (Hellier, 2007; Giovannelli et al., 2012). Another signature of this class of objects is the presence of a strong circular polarization of the emitted light due to cyclotron radiation of charged particles interacting with magnetic field lines. Since the cyclotron emission can be accountable even for half the total light of an *AM Her*, they actually represent the most polarised objects in the sky (Hellier, 2001).

- *IPCV*s or *DQ Her* stars

  DQ Her stars, also known as *Intermediate Polar Cataclysmic Variables* (*IPCV*s), contain an accreting, magnetic, rapidly rotating white dwarf. The white dwarf in *IPCV*s typically has a magnetic field strength ranging between 0.1 and 10 MG (Hellier, 2007), weaker than the field of other classes of *CV*s (e.g. *AM Her* stars). In particular, differently from *AM Her* stars, the field is not strong enough to prevent an accretion disk from forming, but it is capable of disrupting the inner part of the disk where the magnetosphere dominates the accretion. Under these circumstances the Alfvén radius R_A is smaller than the circularization radius R_{circ} but greater than R_{wd}. So, in *IPCV*s, accreting matter follows the magnetic field lines within the magnetosphere delimited by the truncation radius R_d, i.e. where the magnetic pressure is approximately equal to the total gas pressure. Moreover, the moderate magnetic field of the rotating *WD* is unable to trigger the phase-lock between *WD*'s spin and the orbit as typical of *AM Her* stars. Hence, the rotating *WD* is asynchronous with the binary orbital period and $P_{spin} < P_{orb}$. The rotational periods P_{spin} usually range from $33s$ to $2.0hr$, though additional periods can emerge when the rotating searchlight[2] illuminates other structures in the binary (Patterson, 1994; Giovannelli et al., 2012). On the whole, *DQ Her* stars resemble the *AM Her* without spin-orbit synchronism and the absence of a strong circular polarization (Patterson, 1994). Although the *IPCV* class represents only about 5%-10% of Cataclysmic Variables (Patterson, 1994), these stars, with a medium-strength field, combines the characteristics of a non-magnetic system (in its outer regions) with those of a strongly magnetized object (in the region close to the white dwarf). This peculiar feature leads to potentially very complex systems (Hellier, 2001) representing an intriguing middle ground between strongly and weakly magnetized objects.

- *Non-Magnetic CV* stars

  The term "intermediate" for *DQ Her* stars is used because a third class of *CVs* actually exists: the so-called *Non-Magnetic CVs* (*NMCVs*). These stars represent the majority of Cataclysmic Variables and their magnetic field is sufficiently weak that it can be ignored, tipically it's lower than $10^4 G$. In such conditions, the magnetosphere is very small and its radius may coincide with the *WD*'s one. Thus, accretion disk is not truncated and it may extend close to the surface of the *WD* (see Fig. 1.2c).

---

[2]The accretion on the *WD* determines an energy release creating an intense bright spot at one or both *WD*'s magnetic poles. When *WD*'s spin and magnetic axes are not aligned, then the star magnetic field rotates diagonally and may cause a modulation in X-ray/UV/Vis lightcurve due to its lighthouse beam. This phenomenon is a sort of accretion 'footprint' and it is similar to the aurora circling Earth's magnetic poles (Patterson, 1994; Hellier, 2001).

However, due to the several complex and peculiar configurations involved by this systems, it is not surprising that in this classification various classes are not sharply separated. In fact, as showed by Fig. 1.3, the distribution of magnetic field strength for *Polars* and *Intermediate Polars* appears as a continuum of values, even with some overlap (Seward & Charles, 2010).

As stated before, in the present work we are interested in studying *Intermediate Polar* systems. The peculiar nature of these objects allows the formation of an accretion disk internally truncated by the interaction with the magnetosphere and, although they are ubiquitous in astrophysics, nonetheless their dynamics is still not fully understood. Moreover, these systems show a great range of observational clues with periodic and quasi-periodic behaviour, especially in their X-ray emission, on timescales that often are relatively easy to study, making these systems a first choice for understanding the phenomenon of accretion (Hellier, 2007).

1.2.2 X-ray emission

Almost half of the population of *IPCV*s currently known has been discovered through optical observations. However, they are also strong X-ray emitters and the ratio between X-ray and visible flux (F_x/F_v) is greater than unity for this class of stars (Patterson, 1994). These stars are indeed soft X-ray $[0.1 - 2.0]$ keV and hard X-ray $[2.0 - 10]$ keV sources with asynchronous changes of brightness.

Nevertheless, while X-rays from *IPCV*s do exhibit aperiodic variability, this is not the most notable aspect of the X-ray timing properties of these objects. In fact, one of the defining characteristics (if not the defining characteristic) of *IPCV*s is the strictly periodic and coherent X-ray spin modulation. The fundamental criterion in order to define a member of this class is the presence of a rapid and stable periodicity in the light curve of the *CV*. This is typically observed at optical or X-ray wavelengths. The required feature of "rapidity" is non important intrinsically, but it means that $P_{spin} < P_{orb}$, although most stars have $P_{spin} \ll P_{orb}$. On the other hand, the "stability" requirement on long time scale for the period and phase is fundamental in order to discriminate the signals from the several more common phenomena of quasiperiodic oscillations and flickering (Patterson, 1994).

A possible origin for this X-ray emission is the mass accretion (Patterson, 1994). The value of mass accretion rate $\dot{M}$ in *IPCV*s has been inferred from observations through various techniques based on different assumptions [3] , and the expected value of $\dot{M}$ usually

---

[3]Disks with higher $\dot{M}$ in general show higher temperatures and therefore bluer colours. Nevertheless, the B-V and U-B bands show small variations, and even small spurious contributions can produce very large errors in $\dot{M}$. On the other hand, the ultraviolet colours are extremely sensitive to $\dot{M}$, but it is also sensitive to the mass of the white dwarf. This may be the most useful technique but needs a fine calibration.
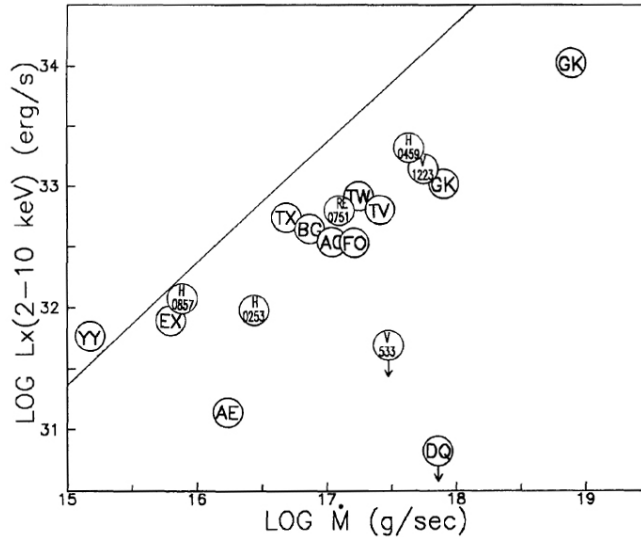
Figure 1.4: L_{hx}, the luminosity in the hard X-ray band $[2.0 - 10]$ keV, vs $\dot{M}$. The continuous thin line represents the prediction from equation (1.3).

ranges between 10^{-11} and 10^{-8} $M_\odot y^{-1}$ (Patterson, 1984, 1994; Giovannelli et al., 2012). According to this finding, we do expect that these objects are strong X-ray emitters. In fact, a significant amount of energy per particle may be released, due to shocks[4] generated by the accreting plasma flowing along the field lines and impacting onto the white dwarf's surface at, approximately, free fall velocity.

Actually, with velocity ranging between 10^8 and 10^{10} cm s^{-1}, the infalling matter moves really fast, compared to the speed of sound, that does not exceed $10^7 cm$ s^{-1}. Therefore, above the star's surface a shock is generated and energy is released by the infalling plasma (Patterson, 1994). The theory predicts that these systems are expected to show an X-ray luminosity given by

$$L_x \approx \frac{GM\dot{M}}{R} \approx 10^{34}\dot{M}_{17} \ erg \ s^{-1}, \tag{1.3}$$

where R is the radius within which the infalling plasma will be guided along the field lines to accrete radially onto the white dwarf, M the star mass, and $\dot{M}_{17}$ is the accretion rate in units of 10^{17} g s^{-1}. To compare this with $[2.0 - 10]$ keV observations, we assume a spectrum with $kT_{brems} = 15$ keV, 50% of the original L_x radiated downward towards the white dwarf, and a white dwarf albedo of 0.3 for hard X rays. According to this model, these impacts should cause a strong emission in the hard X-ray band $[2.0 - 10]$ keV up to $L_{hx} \approx 10^{34}$ erg s^{-1} (Patterson, 1994). In particular, Patterson (1994) derived for several $IPCV$s the mass accretion rate and the expected X-ray emission using the theory

---

[4]A shock wave is a propagating disturbance moving faster than the local speed of sound.

of accreting white dwarf. The comparison of these values with observations has shown that the observed luminosity is systematically lower than expected (see Fig. 1.4). On the whole, the entire *IPCV* class show an X-ray luminosity lower than expected by an average factor of ~ 4, and it is worth noting that this evaluation excludes fast rotators, for which the X-ray underluminosity is even more pronounced (Patterson, 1994). The fact that the observed X-ray flux is significantly lower than the one expected from accretion has defined for many years one of the most compelling issue about this class of stars.

Nonetheless, to date we have an increasingly sophisticated understanding of X-ray emission from radial accretion onto white dwarfs, and this has successfully been used to estimate the white dwarf mass in many cases (e.g., Ramsay et al., 1998). The fact that these X-rays are emitted close to the white dwarf surface is established also by the detection of strong reflection signal, that is X-rays emitted downward just above the white dwarf surface, then scattered off it (Mukai et al., 2015). Moreover, *PCV*s do not have an accretion disk, but a subset of them have strong hard X-ray component. When they do, their X-ray spectra are similar to those of *IPCV*s (Ishida et al., 1997). Furthermore, they are often subject to self-occultation (i.e., being blocked by the body of the white dwarf when the emission region goes behind it), so we know the location and approximate size of the emission region. Finally, there is one *IPCV* (*XY Ari*) which is relatively X-ray bright and deeply eclipsing. The eclipses are sharp, which means that the X-ray emission region is very compact (a fraction of the white dwarf) (Hellier, 1997).

1.2.3 Flickering

Another intriguing feature shared by all the *CV* stars, including *IPCV*s, is the *flickering*, i.e. a random, broad-band and short term modulation of luminosity. It appears as a sequence of overlapping flares and bursts apparently having no cycle or periodicity. This phenomenon has been observed in the X-ray light curves of *CV*s of all classes, and ranges from fluctuations lasting few seconds to larger changes in brightness with rises and dips lasting for hours, with no pattern or period.

Despite flickering has been studied for a long time, especially in the visible region of the electromagnetic spectrum, its origin is still uncertain (Tamburini et al., 2009). In order to find out where flickering comes from, it may help compare the lightcurve of two different *CV*s (see Fig. 1.5). The first one is a the lightcurve of *U Gem* (a dwarf nova) showing that the flickering disappears during eclipse. Since this system is thought to have grazing eclipses, the secondary star hides the white dwarf leaving the inner region of the accretion disk visible. This implies that the flickering of *U Gem* arises from a bright spot on the surface of the compact object, where the accreting material from the disk impacts on.

The second lightcurve has been observed from *HT Cas* (another dwarf nova) and shows a completely different scenario. In this lightcurve flickering resumes before the egress of the bright spot on the white dwarf's surface. This demonstrates that in this system the flickering arises in the inner region of the accretion disk, close to the white dwarf.

Thus, from comparisons like this we can infer that flickering may arise in the turbulent inner region of the disk, or from the bright spot on the surface of the white dwarf (Hellier, 2001). Actually, since the mid 80s the analysis of eclipsing lightcurve of the *CV RW tri* (a Nova-like star) (Horne & Stiening, 1985) demonstrated that the flickering source must be concentrated in the centre of the accretion disk but it is not necessarily confined to the immediate vicinity of the white dwarf, possibly spreading out in the inner part of the accretion disk (Bruch, 2015). In this respect it is worth noting that the differential rotation of the disk together with the interaction of the disk with a strong magnetic field may cause magnetic reconnection close to the disk surface (Galeev et al., 1979), just in the inner turbulent region of the disk, where the observations suggest that phenomena responsible of *flickering* may occur (Hellier, 2001; Seward & Charles, 2010).

In the light of these considerations, it is plausible that the X-ray emission observed in some of the *IPCV* stars may have a thermal component due to a coronal activity occurring on the surface of the accretion disk. Actually, some authors suggest that a coronal activity occurring on the surface of accretion disk, could develop and sustain an extended corona between star and disk (e.g. Favata et al., 2005; Orlando et al., 2011), although these authors referred to star-disk systems with a not-compact star.
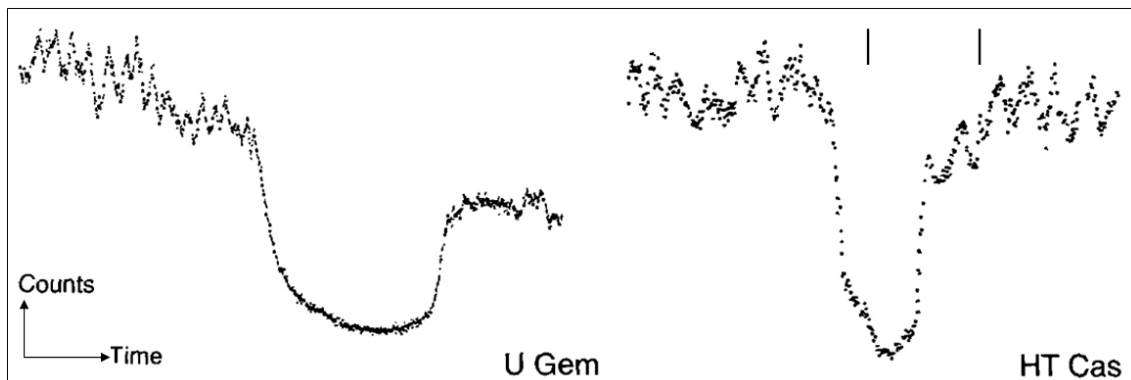

Figure 1.5: The lightcurve of *U Gem* shows a grazing eclipse of the bright spot only, the contextual disappearance of flickering indicates that it originates in the bright spot. The lightcurve *HT Cas* shows that flickering resumes before the egress (right hand tick) of the bright spot of the white dwarf, thus it must arise in the inner disk (Hellier, 2001).

1.2.4 Period changes and torques theory

Section 1.2.2 emphasized the importance of the spin period of the star (P_{spin}) and its comparison with the orbital period of the binary system (P_{orb}). Nevertheless, P_{spin} is not immutable and the white dwarf can spin up or down. In general, due to a moment of inertia sufficiently small, magnetic white dwarfs may experience torques from the disk able to produce measurable spin period changes. This effect is often addressed as "matter torque" (Patterson, 1994). It is an expected behaviour that the white dwarfs of *IPCV* spin up due to angular momentum accreting from the disk. Nonetheless, this argument is not always true, since some stars are spinning down, and several other stars are rotating too slowly to have gone through a spin-up over a long period of time. The theory of Ghosh & Lamb (1978) showed that a magnetic compact star accreting matter from a disk may abide a total torque more complex than the above mentioned "matter torque".

According to this theory, the rotating white dwarf is characterized by a "fastness parameter" ω_s. This parameter is defined as $\omega_s = \omega_*/\omega_d$, where ω_d is the angular velocity at the magnetospheric radius[5] (i.e. the truncation radius R_d). When $\omega_s \approx 0$ the star is considered a "slow rotator" and the matter torque dominates. Otherwise, when $\omega_s > 0$, the white dwarf is a "fast rotator". In this configuration, some of its field lines stick in the more slowly rotating disk, exerting a spindown torque opposing the matter torque. When ω_s approaches a critical value ($\omega_{crit} = 0.35 - 0.85$), the spin-down torque may exceed the matter torque determining a spin equilibrium. For $\omega_s > \omega_{crit}$, the star should spin down, and accretion could be subdued (Patterson, 1994).

1.3 Open issues and approach

To date it is a largely accepted idea that flare may occur on the surface of accretion disks of stellar objects. The theoretical studies conducted by Galeev et al. (1979) showed that a conspicuous formation of magnetic loops may occur on the surface of accretion disks, due to the interaction between the magnetic field of the central star and the differentially rotating disk. Therefore, such a context is amenable to triggering a flaring activity involving the surface of the disk. After all, the conditions required to cause flares exist on the surface of an accretion disk. As a matter of fact, we are in the presence of a magnetized disk

---

[5] The magnetospheric radius is defined as the radius where the magnetic torques equal the internal viscous torques in the disk (Bessolaz et al., 2008). This criterion gives an upper limit for the R_d, as it only defines a radius where the star-disk interaction starts to affect accretion (e.g. Armitage & Clarke, 1996). A more conservative approach, giving a lower limit for R_d, states that accretion funnels take place when accretion is no longer possible because of the overwhelming field strength, i.e. when $\beta = 1$, see equation 1.1 (e.g. Romanova et al., 2002).

in differential motion (e.g. quasi-keplerian), where plasma pressure largely overwhelms magnetic pressure. In the accretion disk, in fact, plasma is in a condition similar to the one found in solar chromosphere where indeed flaring activity is normally observed.

Observations conducted on $CTTS$ in the context of project COUP (Chandra Orion Ultradeep Project) demonstrated clear evidence of extended ($l > R_*$) flares confined by magnetic field structure. Such phenomena, due to their inferred size, cannot be limited to the star surface and must extend beyond, connecting star and accretion disk (Favata et al., 2005). Moreover, some magnetohydrodynamic models predict that flaring activity close to, or on, the disk may trigger accretion phenomena (Orlando et al., 2011).

For the above reasons, it is arguable that the events observed in $CTTS$ during the COUP project, may reasonably occur in compact systems like $IPCV$ as well. Moreover, in these compact systems, due to stronger magnetic field intensity close to the star, flaring activity may be scaled to an energy budget of several order of magnitude higher compared to flares occurring in $CTTS$. Additionally, this extended coronal activity occurring on the disk may produce thermal X-ray emission contributing significantly to the coronal component of $IPCV$s.

This thesis addresses the effects of coronal activity occurring on the accretion disk of compact objects, in particular the $IPCV$ class. The main questions we want to answer are: what happens if a flaring activity occur on the accretion disk surface of a $IPCV$? Under which condition the stability of the system may be compromised? Can flares build up and sustain an extended corona above the disk? Is this coronal activity contributing to the thermal X-ray emission observed from these object?

With these questions in mind, we have developed a model taking into account all the key physical processes, including gravity, disk viscosity, thermal conduction, radiative losses from optically thin plasma and coronal heating. Then, we performed 3D magnetohydro-dynamic simulations in order to investigate if the energy released by several flares on the surface of the disk of a $IPCV$ may contribute to the formation of an extended corona at temperature of the order of 10^8 K above the accretion disk. Finally we synthesized the thermal X-ray emission due to this coronal activity along with its variability and compared it with some observed features.

In Chapter 2 we describe the magnetohydrodynamic model and the numerical setup; in Chapter 3 we report the results in terms of the dynamics of the system and thermal X-ray emission; in Chapter 4 we draw our conclusions and discuss the future perspectives of the present work.

Chapter 2

Model and numerical setup

2.1 The MHD Model

The model describes an intense flaring activity taking place on the surface of the accretion disk placed around a rotating magnetized compact object. The stellar system taken into account is a prototype of *IPCV*. The central compact object is surrounded by a structured atmosphere initially unperturbed and approximately in equilibrium. In order to study *IPCV*s, we adapted the model described in Orlando et al. (2011) developed for *Classical T-Tauri Stars* (*CTTS*).

2.1.1 MHD equations

The system evolution can be described through the four time-dependent classical MHD equations, extended to include gravitational force, viscosity, thermal conduction, radiative cooling and plasma heating. These equations are defined in a 3D spherical coordinate system (r, θ, ϕ) and they are here reported in c.g.s. in the conservative form with source terms (see Appendix C.1):

$$\frac{\partial \rho}{\partial t} + \nabla \cdot (\rho \vec{u}) = 0 \qquad\qquad \textit{Mass conservation eq.}$$

(2.1)

$$\frac{\partial \rho \vec{u}}{\partial t} + \nabla \cdot (\rho \vec{u} \vec{u}) = -\nabla p + \left(\frac{\vec{j} \times \vec{B}}{c} \right) + \nabla \cdot \vec{\tau} + \rho \vec{g} \qquad \textit{Momentum conservation eq.}$$

(2.2)

$$\frac{\partial \varepsilon}{\partial t} + \nabla \cdot (\varepsilon \vec{u}) = -\nabla \cdot (p \vec{u}) + \vec{u} \cdot \left(\frac{\vec{j} \times \vec{B}}{c} \right) + \nabla \cdot (\vec{u} \cdot \vec{\tau})$$

$$+ \rho \vec{u} \cdot \vec{g} - \nabla \cdot \vec{F_c} - n_e n_H \Lambda(T) + Q(r, \theta, \phi, t) \qquad \textit{Energy conservation eq.}$$

(2.3)

$$\frac{\partial \vec{B}}{\partial t} = -c\nabla \times \vec{E} = \nabla \times \left(\vec{u} \times \vec{B}\right) \qquad\qquad\qquad\qquad \textit{Induction eq.}$$

(2.4)

where the p is the thermal pressure for a fully ionized plasma, and the total energy per unit volume (ε) is the sum of internal or thermal (ε_i) and kinetic energy (E_k), with $\gamma = 5/3$:

$$p = 2n_H k_B T; \qquad\qquad \varepsilon = \varepsilon_i + E_k = \frac{p}{(\gamma - 1)} + \rho\frac{\vec{u}\cdot\vec{u}}{2}. \qquad (2.5)$$

The mass density is defined as $\rho = \mu m_H n_H$, where m_H is the mass of hydrogen atom, n_H is the number of hydrogen atoms per unit of volume, and $\mu = 1.28$ (assuming metal abundances of 1, equal to solar ones) is the mean atomic mass (Anders & Grevesse, 1989). The bulk velocity of the plasma is defined as $\vec{u}$. Moreover, the equation (2.4) has been taken in its ideal form for high *magnetic Reynolds number* ($R_m \gg 1$). On this regard, we should point out that the system we are modeling is intimately related to phenomena for which non-ideal MHD has a crucial role. In fact, magnetic reconnection is thought to be the fundamental mechanism behind flares and during flares the magnetic energy is released through ohmic and anomalous resistivity (see Appendix B). Nevertheless, magnetic reconnection is a local phenomenon that requires a resolution far higher than that considered in our model, in order to simulate and resolve the fine structure of the single twisted coronal loop (e.g. Reale et al., 2016). With this in mind, we are not interested in studying the mechanism behind the energy release through magnetic reconnection, however, we focused our study on the effects of an intense flaring activity on the disk dynamics and on the formation of an extended corona.

2.1.2   Viscosity

We take into account in our model the turbulent viscosity of the disk following the α-model of Shakura & Sunyaev (1973) where the turbulence in the plasma is considered the source of an increased viscosity, and the angular momentum transport due to turbulence is parametrized through α. The viscosity is taken into account in MHD equations through the viscous tensor $\vec{\tau}$ (see Appendix A). The viscosity is assumed to be effective only in the circumstellar disk and negligible in the region of the extended corona (Orlando et al., 2011; Giovannelli et al., 2012). The technique used to track the disk material, where viscosity is effective, is based on the definition of a tracer following the same evolution of density (i.e. the tracer is passively advected similarly to the density). We defined the tracer C_d as the disk mass fraction inside each computational cell, initializing at $t = 0$ (initial condition)

the disk material with $C_d = 1$ and the extended corona with $C_d = 0$. During the evolution of the system, the tracer is let evolve advecting similarly to the density (i.e. C_d is not constant). Then the viscosity is enabled only in the computational cells containing at least 99% of material of the disk (i.e. $C_d > 0.99$). The viscous stress tensor is defined as:

$$\vec{\tau} = \eta_v \left[(\nabla \vec{u}) + (\nabla \vec{u})^T - \frac{2}{3} (\nabla \cdot \vec{u}) \vec{I} \right] \tag{2.6}$$

where dynamic (or shear) viscosity η_v is proportional to density through kinematic viscosity ν_v as follows:

$$\eta_v = \nu_v \rho = \rho \alpha \frac{c_s^2}{\Omega_k} \tag{2.7}$$

where $c_s = \sqrt{\frac{\gamma p}{\rho}}$ is the isothermal sound speed and Ω_k is the angular velocity of the circumstellar disk in quasi-Keplerian rotation. α is a phenomenological dimensionless parameter defined in the Shakura & Sunyaev model taking into account the effect of anomalous viscosity (Shakura & Sunyaev, 1973). In this model α can be assumed to be a measure of the strength of the turbulent angular momentum transport and varies in the range $0.01 - 0.6$ (Balbus, 2003). In the simulations here presented, we assumed constant $\alpha = 0.02$ (Romanova et al., 2002).

2.1.3 Thermal conduction

Thermal conduction appears in the energy equation (2.3) as minus the heat flux divergence $(-\nabla \cdot \vec{F_c})$. In accordance with the standard formulation by Spitzer (Spitzer, 1962), thermal conduction is highly anisotropic due to the presence of the magnetic field that drastically reduces the conductivity component transverse to the field. As a matter of fact, thermal flux can be locally splitted in two components, one along and the other across the magnetic field lines:

$$\mathcal{L}_c = -\vec{\nabla} \cdot \vec{F_c} = -\vec{\nabla}_\parallel \cdot \vec{F}_\parallel - \vec{\nabla}_\perp \cdot \vec{F}_\perp. \tag{2.8}$$

The two components of thermal flux can therefore be written as

$$\begin{aligned} F_\parallel = [q_{spi}]_\parallel = -k_\parallel \left(\vec{\nabla}_\parallel T \right) \approx -9.2 \cdot 10^{-7} T^{\frac{5}{2}} \left(\vec{\nabla}_\parallel T \right) \\ F_\perp = [q_{spi}]_\perp = -k_\perp \left(\vec{\nabla}_\perp T \right) \approx -3.3 \cdot 10^{-16} \frac{n_H^2}{T^{\frac{1}{2}} B^2} \left(\vec{\nabla}_\perp T \right) \end{aligned} \tag{2.9}$$

where $k_\parallel$ and $k_\perp$ are the thermal conduction coefficients along and across field lines (in units of $erg s^{-1} K^{-1} cm^{-1}$). From equations (2.9) it is clear that, if the magnetic field is sufficiently strong, the ratio $\frac{k_\perp}{k_\parallel} \ll 1$ and thermal conduction behaves anisotropically working prevalently along field lines. Moreover, the classical theory of thermal conduction is based on the assumption that the mean free path λ is smaller than the temperature scale height L_T, and when the requirement

$$\lambda \ll L_T = \frac{T}{|\nabla T|} \tag{2.10}$$

is not fullfilled, the equation (2.8) overestimates thermal flux. When fast phenomena occur, like flares in their early phases, it is well known that rapid transients, fast dynamics and steep gradients develop (Reale & Orlando, 2008). So, under these circumstances, Spitzer's heat conduction formulation breaks down becoming flux limited, and therefore cannot be suitable (Brown et al., 1979). For this reason the two components of thermal conduction must be redefined as follows (Orlando et al., 2008):

$$
\begin{aligned}
F_\parallel &= \left(\frac{1}{[q_{spi}]_\parallel} + \frac{1}{[q_{sat}]_\parallel} \right)^{-1} \\
F_\perp &= \left(\frac{1}{[q_{spi}]_\perp} + \frac{1}{[q_{sat}]_\perp} \right)^{-1}
\end{aligned}
\tag{2.11}
$$

where the saturated heat flux along and across field lines are (Cowie & McKee, 1977)

$$
\begin{aligned}
[q_{sat}]_\parallel &= -sign\left(\vec{\nabla}_\parallel T\right) \cdot 5\varphi\rho c_s^3 \\
[q_{sat}]_\perp &= -sign\left(\vec{\nabla}_\perp T\right) \cdot 5\varphi\rho c_s^3
\end{aligned}
\tag{2.12}
$$

φ is a parameter we set equal to unity (Giuliani, 1984; Borkowski et al., 1989; Fadeyev et al., 2002).

2.1.4   Radiative cooling

The amount of energy lost through radiative cooling can be taken into account in the energy equation (2.3) as a radiative loss function defined as minus the divergence of a radiative flux (Priest, 2014). It can be written in the following simple form

$$\mathcal{L}_r = -\vec{\nabla} \cdot \vec{F}_r = -\vec{\nabla} \cdot \left(-k_r \vec{\nabla} T\right) = k_r \vec{\nabla}^2 T \tag{2.13}$$

if the coefficient of radiative conductivity $k_r = 16\sigma_s T^3/(3\tilde{\kappa}\rho)$ is locally uniform. Where σ_s is the Stefan-Boltzmann constant, $\tilde{\kappa}$ the opacity or mass absorption coefficient, and $\tilde{\kappa}\rho$ is the absorption coefficient.

For optically thin plasma of the stellar atmosphere ($T \gtrsim 2 \cdot 10^4 K$ in the solar chromosphere and corona), the radiative loss function $\mathcal{L}_r$ is no longer coupled to the radiation field through the radiative transfer mechanism and it takes the form

$$\mathcal{L}_r = -n_e n_H \Lambda(T) = -n_H^2 \Lambda(T) \tag{2.14}$$

where $\Lambda(T)$ represents the optically thin radiative losses per unit emission measure, n_e is the electron density and n_H the density of hydrogen atoms or protons for a fully ionized plasma ($n_e = n_H$). In our model the effects of radiative cooling are actually considered through the term in the right hand side of equation (2.14) in energy conservation equation (2.3).

2.1.5 Coronal heating and flaring activity

The coronal heating has been prescribed as a phenomenological term, composed of two components. The first one works at temperature $T \leq 2\,10^4 K$ and balances exactly the local radiative losses. Nevertheless, several tests on the $3D$ simulations showed that increasing this value to $T \leq 1\,MK$ determines a way more stable calculation and significant reduction of computational costs with comparable results in terms of dynamics of the plasma and thermal X-ray emission. The second component is transient and consists of flares (see Appendix B) occurring on the surface of the disk. Every single flare is simulated and triggered injecting energy in the system through a heat pulse. We considered the release of several flares with a randomly generated timing in order to achieve a frequency ranging from approximately 1 flare every 2.5 seconds to 1 flare every 100 seconds (Tamburini et al., 2009). The location of every heat pulse is randomly chosen in an angular interval $\delta\theta \approx 3°$ reckoned from the accretion disk surface. The area subject to flaring activity is the annular region between $90R_*$ and $216R_*$. This assumption stems from an observation concerning the measurement of the size of accretion disk coronae, based on ingress/egress timing, in another but similar context (Church & Bałucińska-Church, 2004). The 3D spatial distribution of each pulse is defined to be gaussian with a width of $\sigma = 5 \cdot 10^8 cm$. The total time duration of every pulse is set at $100s$, afterwards the pulse is completely switched off. The time evolution of pulse intensity is divided in three equally spaced parts: a linearly increasing ramp, a steady part and a linearly decreasing ramp. The energy is injected with a maximum intensity of $H_0 = 2 \cdot 10^5 erg \cdot cm^{-3} \cdot s^{-1}$. This value of power per unit volume

yields a maximum total energy of a single flare of $E_{fmax} \approx 10^{34} erg$. As a conservative choice we have taken values typical of large solar flares (Priest, 2014). Nevertheless the effective intensity of flares has been randomly generated with a power law with $\alpha = -2.1$ (Priest, 2014), approximating the intensity distribution of flares on the Sun (see Appendix C.4).

2.2   Barotropic stellar atmosphere

Most *IPCV*s have a $0.8 - 0.9 M_\odot$ white dwarf for which an appropriate radius is $R_* = 6.0 \cdot 10^8 cm$ (i.e. $10^{-2} R_\odot$). Nevertheless, being aware of this, we deliberately decided to consider a star more massive, with a mass at the limit of its class. This choice has been made in order to have a more rapidly evolving system, due to higher orbital velocity, thus reducing computational costs. For these reasons, we located a compact object of mass $M_* \simeq 1.4 M_\odot$ (Putney, 1999), radius $R_* = 6.0 \cdot 10^8 cm$ and spin period of 5.4 minutes (Patterson, 1994; Norton et al., 1999) at the origin of a 3D spherical coordinate system.

The magnetic field generated by the white dwarf is supposed to be in a force-free dipole-like initial configuration with the magnetic dipole aligned with the rotation axis of the star (Hellier, 2007). The dipolar magnetic field may be decomposed in two components in spherical coordinate as follows:

$$B_r = \frac{2\mu_B}{r^3} cos\theta, \qquad\qquad B_\theta = \frac{\mu_B}{r^3} sin\theta. \qquad (2.15)$$

The magnetic moment μ_B has been chosen so as to get the desired magnetic field intensity at the stellar surface B_{sup}, ranging between $1.5 \cdot 10^5 G$ and $10^7 G$ in the several configurations explored (see Table 3.1). The magnetosphere is defined as a quasi-cylindrical region of radius equal to the truncation radius R_d where the disk structure begins in the equatorial plane. This region, surrounding the central star, is assumed to rotate as a rigid body with the same angular velocity of the star ($\omega_* = \omega_{mag}$) (see Fig. 2.1a and 2.2c).

The accretion disk in our model consists of relatively cold ($T_d \approx 5 \cdot 10^4 K$) isothermal plasma rotating with angular velocity close to the Keplerian value[1]. Disk density is structured in order to follow the barotropic prescription (see below) and has been chosen in order to get an inner disk particle density n_d ranging between $\approx 10^{10} cm^{-3}$ and $\approx 10^{14} cm^{-3}$ in the various system configurations considered (see Table 3.1). The disk is initially truncated

---

[1]We defined a correction factor $k = 1.01$ as in Romanova et al. (2002) and Orlando et al. (2011), see below.
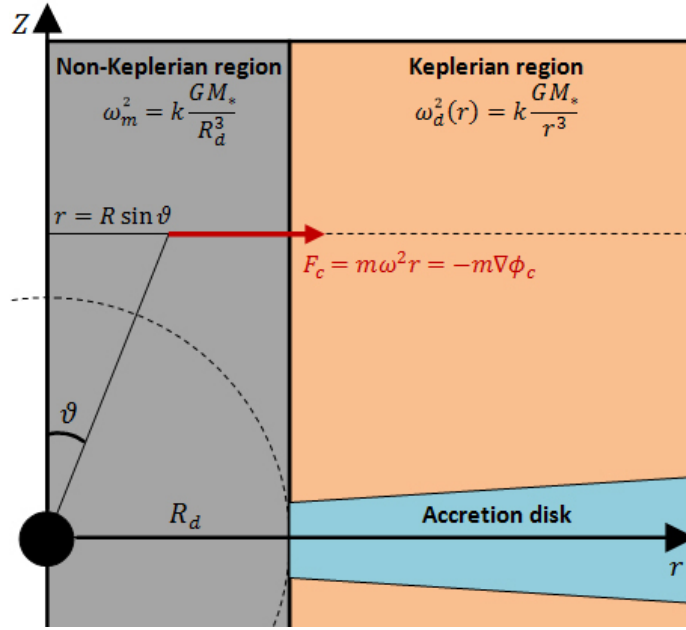
(a)
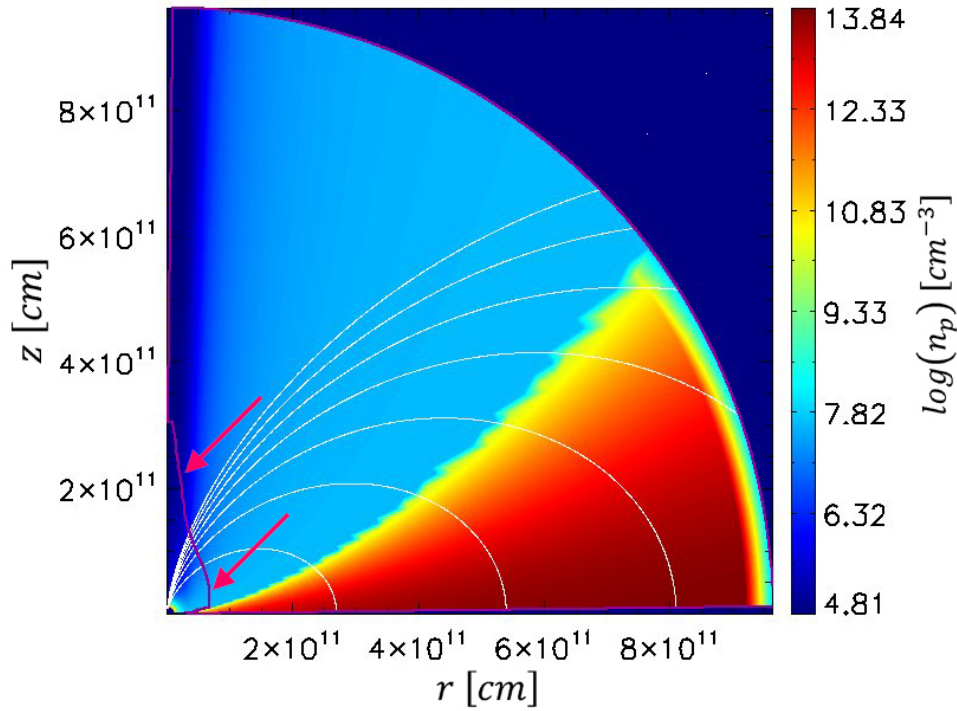
(b)

Figure 2.1: (a) Scheme of the cross section of the differentially rotating domain regions and definition of some physical quantities; (b) colour-coded log scale of density distribution in the computational domain used in the preliminary 2.5D simulation. White lines represent projected magnetic field lines, whilst the magenta line (marked by arrows) is the $\beta = 1$ surface (run F4f1.00a).
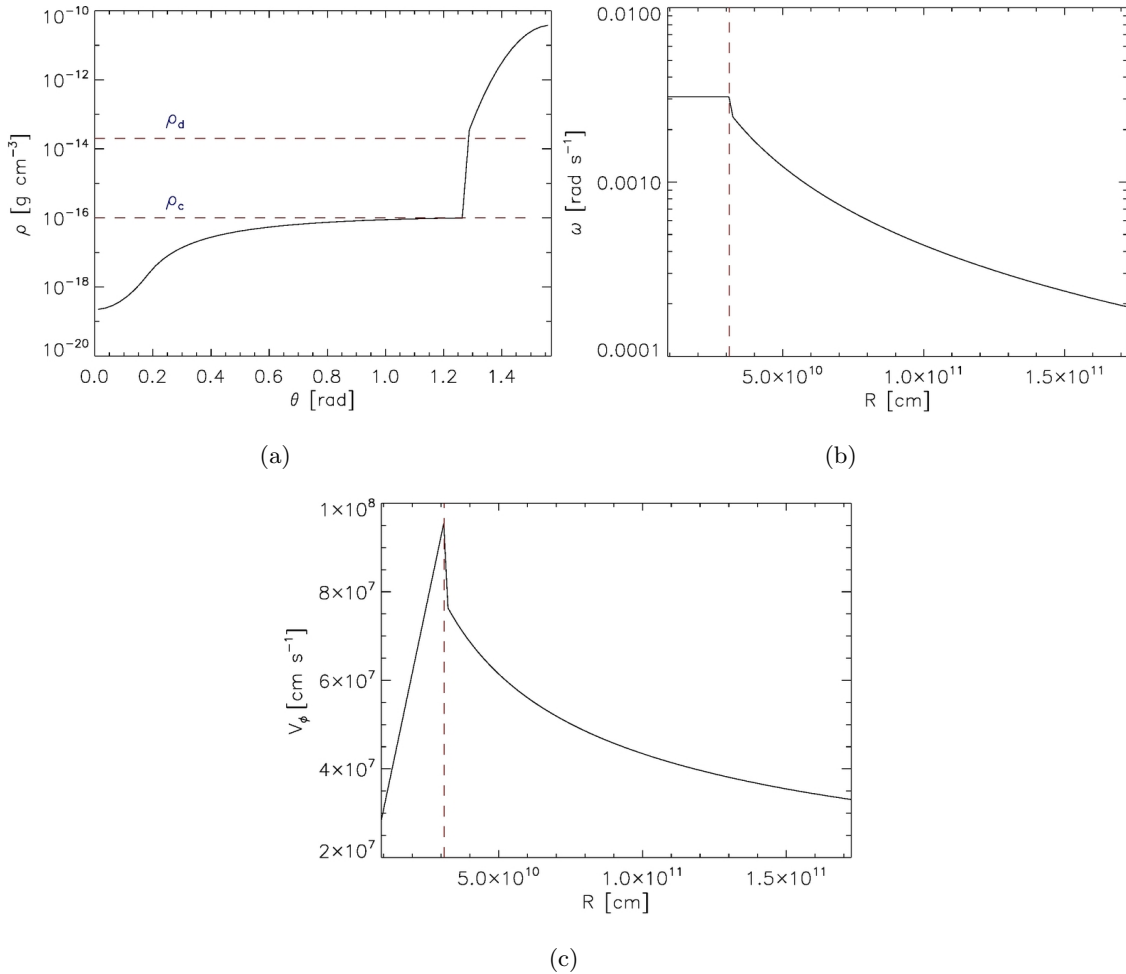
(a)

(b)

(c)

Figure 2.2: Distribution of some physical quantities: (a) density profile along a spherical surface for fixed radius ($R = 1.7 \cdot 10^{11}$ cm) and for θ between $0°$ (rotation axis) and $90°$ (equatorial plane), the horizontal dashed lines represent the density of the disk (ρ_d) and the corona (ρ_c) at the contact layer; (b) angular and (c) rotation velocity of the disk in the equatorial plane, the vertical dashed lines identify the truncation radius (R_d) (run F4f1.00a).

by the stellar magnetosphere at the truncation radius R_d, where there is equilibrium between plasma and magnetic pressure and therefore the ratio of the plasma pressure to the magnetic pressure, $\beta = 8\pi(p + \rho v^2)/B^2$, is close to unity. In accordance with the others parameters chosen, R_d has been placed at $45R_*$ from the center of the star (Hellier, 1993). In this regard, it is worth noting that in all the simulations run the magnetic field and the disk density have been changed so as to keep R_d constant. The corotation radius, where plasma rotates at the same angular velocity of the star, is imposed to be identical to the truncation radius, i.e. $R_{cor} = R_d$. This is obtained choosing the angular velocity of the star ω_* (and, consequently, of the rotating dipole-like magnetic field) so as to be equal to the angular velocity of the plasma at the truncation radius $\omega_d(R_d)$. This assumption is

based on the belief that most intermediate polars are in a sort of rotational equilibrium (Warner, 1996; Norton et al., 1999). Basically, the accretion disc is disrupted at the radius (R_d) where the Keplerian rotation of the disk is equal to that of the white dwarf, that is $\omega_* = \omega_d(R_d)$.

The extended corona is a shell of optically thin and hot gas above the accretion disc (Giovannelli et al., 2012). In our model this region has a density following barotropic prescription (see below), whilst temperature is imposed to be initially uniform and equal to $T_{cor} = 10^7 K$, defining an isothermal low density region extending above the surface of the disk and connecting it with the central star.

In order to define a circumstellar medium in a quiescent configuration, we adopted the barotropic conditions introduced by Romanova et al. (2002). These initial conditions satisfy mechanical equilibrium involving centrifugal, gravitational, and pressure gradient forces. Generalizing hydrostatic balance equation, we can consider different contributions to the force, beyond the gravitational one:

$$\vec{\nabla}p = -\rho a_{gen} = \rho\vec{\nabla}\mathcal{F} = \rho\vec{\nabla}\left(\phi_{kep} - \phi_g - \phi_c\right). \tag{2.16}$$

The various contributions to the $\mathcal{F}$ function are gravitational (ϕ_g), centrifugal (ϕ_c), and a non-Keplerian correction (ϕ_{kep}). They are defined as follows:

$$\phi_{kep} = (k-1)\frac{GM_*}{R_d}; \tag{2.17a}$$

$$\phi_g = \frac{GM_*}{r}; \tag{2.17b}$$

$$\phi_c = \begin{cases} -\int_\infty^{R_d}\omega_d^2 r\ dr \quad -\int_{R_d}^{r}\omega_m^2 r\ dr \\ \qquad\qquad = k\frac{GM_*}{R_d}\left[1 + \frac{R_d^2-r^2}{2R_d^2}\right] \qquad (r \le R_d) \\ \\ -\int_\infty^{r}\omega_d^2 r\ dr \quad = k\frac{GM_*}{r} \qquad\qquad (r \ge R_d). \end{cases} \tag{2.17c}$$

Where $r = Rsin\theta$ is the cylindrical radius and $k = 1.01$ is a parameter taking into account that the disk is slightly non-Keplerian. Moreover, (see Fig. 2.1a and 2.2b) the angular velocity of the plasma is given by

$$\omega^2 = \begin{cases} \omega_m^2 = k\frac{GM_*}{R_d^3} & (r \le R_d) \\\\ \omega_d^2 = k\frac{GM_*}{r^3} & (r \ge R_d). \end{cases} \tag{2.18}$$

In equation (2.18) we distinguish ω_m, the angular velocity of magnetosphere, where plasma is rotating as a rigid body, from ω_d, the angular velocity of the quasi-Keplerian region. Taking coronal density (ρ_c) and disk density (ρ_d), both at disk surface, and coronal temperature (T_c), as input parameters (see Table 3.1) and using the perfect gas law $\left(p = \frac{2\rho k_b T}{\mu m_H}\right)$, we can compute the pressure at the contact layer between the corona and disk:

$$p_0 = \frac{2\rho_c k_b T_c}{\mu m_H}$$

$$p_0 = \frac{2\rho_d k_b T_d}{\mu m_H} \qquad \Rightarrow \qquad T_d = \frac{p_0 \mu m_H}{2\rho_d k_b}. \tag{2.19}$$

Finally, equation (2.16) yields pressure as a function of $\mathcal{F}$

$$\vec{\nabla}p = \rho\vec{\nabla}\mathcal{F} = p\frac{\mu m_H}{2k_b T}\vec{\nabla}\mathcal{F} \qquad \Rightarrow \qquad \int_{p_0}^{p}\frac{dp}{p} = \frac{\mu m_H}{2k_b T}\int_{0}^{F}d\mathcal{F}$$

$$\Rightarrow \quad p = p_0 e^{\mathcal{F}\frac{\mu m_H}{2k_b T}}. \tag{2.20}$$

and finally we get pressure and density as follows

$$p = \begin{cases} p_0 e^{\mathcal{F}\frac{\mu m_H}{2k_b T_c}} & Corona \\\\ p_0 e^{\mathcal{F}\frac{\mu m_H}{2k_b T_d}} & Disk \end{cases} \qquad \rho = \begin{cases} p\frac{\mu m_H}{2k_b T_c} & Corona \\\\ p\frac{\mu m_H}{2k_b T_d} & Disk \end{cases} \tag{2.21}$$

From these values we obtain an analytic function describing density and pressure in the whole domain taken into account.

2.3 Initial and boundary conditions

Barotropic initial conditions along with a dipole-like magnetic field configuration may be considered an useful analytic description of a quasi equilibrium system. Nevertheless, due to the interaction with the disk, where $\beta > 1$ and plasma dynamics dominates, the magnetic

field is strongly influenced by the keplerian rotation of the disk. Consequently, after a certain amount of time, the magnetic field is expected to be deformed and put into a coil shape due to the interaction with the disk. In order to get a configuration of the system as much realistic as possible, we divided the numerical simulations in two distinct steps.

As a first step, we have run several 2.5D simulations[2] with a square computational domain of 114×64 cells in spherical coordinates (r, θ) and initial conditions defined by equations (2.16 - 2.21). The radial direction has been discretized on a grid with space steps increasing exponentially with R. The domain extends from $R_{min} = 15R_*(\approx 9 \cdot 10^9 cm)$ to $R_{max} = 3000R_*(\approx 1.8 \cdot 10^{12} cm)$. With this choice, the inner boundary does not coincide with the stellar surface and, therefore, the region closer to the star is not taken into account in our simulations. We made this choice for two main reasons: first, this region has not a relevant impact on our study, which is rather focused on the evolution of the region above disk surface; second, in this way we avoid computational cells having very small $\delta\theta$ mesh size, because they dramatically increase the computational time. The radial grid is made of $n_r = 114$ points with a maximum resolution of $\Delta R = 4.2 \cdot 10^8 cm$, close to the star, and $\Delta R = 8.2 \cdot 10^{10} cm$, at the external end of the domain. The disk has been externally truncated at $R = 9 \cdot 10^{11} cm$, i.e. approximately at half radial domain. The boundary conditions at R_{min} (i.e. at the end close to the star) are assumed so that infalling material follows field lines, passing through the surface of the boundary as an outflow (Romanova et al., 2002). At R_{max} zero-gradient boundary condition is assumed. As for the angular coordinate θ, it ranges from $0°$ (rotation axis) to $90°$ (equatorial plane) and has been discretized uniformly using $n_\theta = 64$ points, giving a resolution of $\Delta\theta \sim 1.4°$. For $\theta = 0°$ (i.e rotation axis) axisymmetric boundary conditions are assumed; i.e. we prescribe a sign change across the boundary of all vectorial components, except for components along the axis itself. For $\theta = 90°$ (i.e equatorial plane) equatorial-symmetric boundary conditions are assumed; i.e. we prescribe a sign change across the boundary of the normal component of velocity and of the component of the magnetic field tangential to the interface. We let the magnetic field interact with the disk for almost 2.5 hrs of physical time so as to reach an almost steady state configuration. It is worth noting that, in this preliminary step of the implemented two-phases technique, the whole size of the domain and disk has been intentionally overestimated in order to avoid undesired boundary effects during the evolution of the system. In fact, several tests showed that the prescription of a zero-gradient boundary condition (i.e. an "outflow b. c.") at the outer end of the disk might not reproduce correctly the dynamics of the plasma resulting in an underestimate of the

---

[2]In the 2.5D formalism integration is performed in a bi-dimensional domain, along the first two coordinates (say x; y), but the vectorial quantities (i.e velocity, magnetic field) of the fluid have non-vanishing component along the third dimension.

plasma inflow. To this end, in the following phase we take into account only the inner part of the 2.5D domain (see Fig. 2.3).
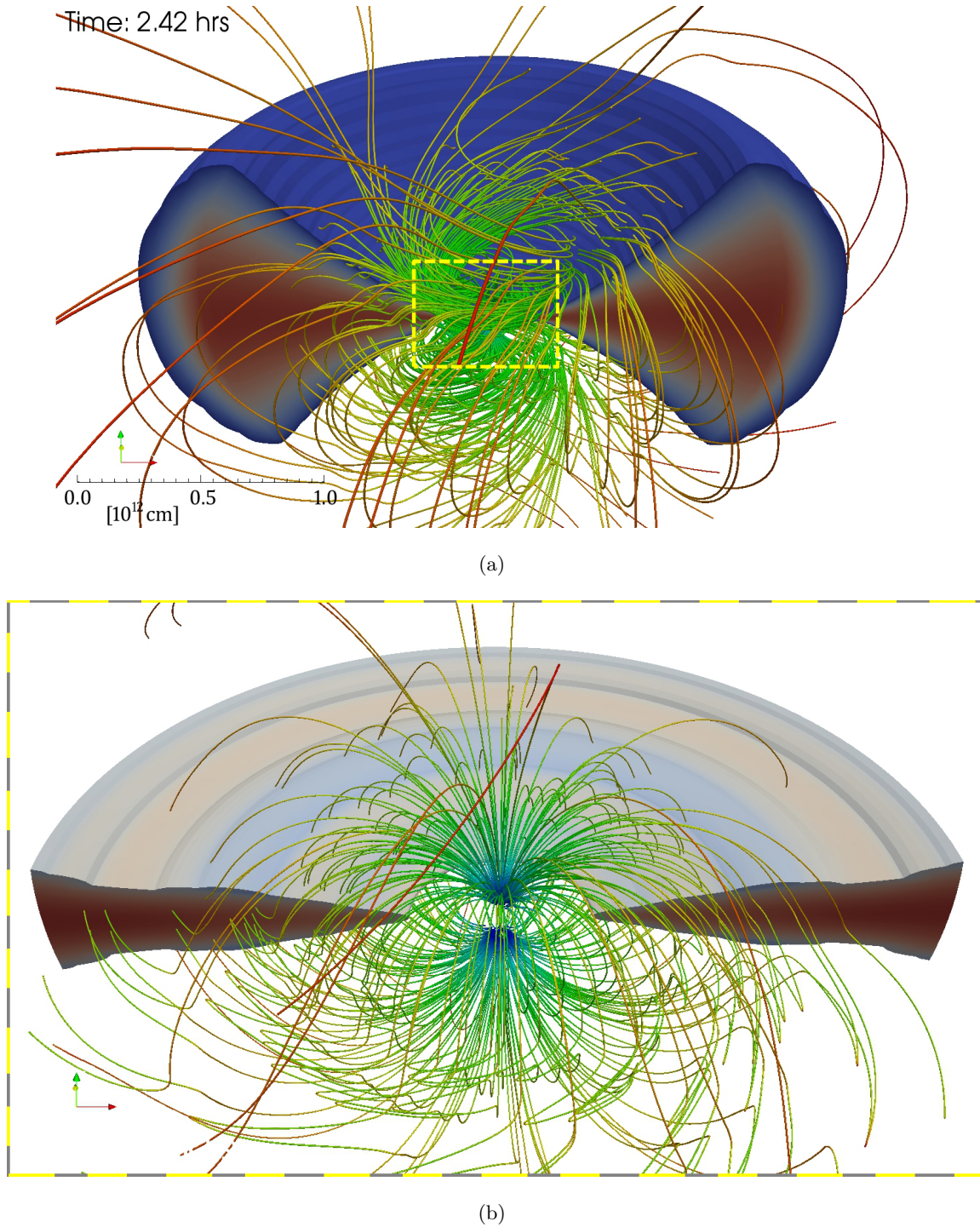

(a)

(b)

Figure 2.3: Result of the simulation to generate the initial configuration of the 3D simulation: (a) cutaway view of the 3D reconstruction of the 2.5D simulations after 2.5 *hrs* with a fully developed magnetic field, the yellow box contains the region mapped in 3D and used as initial condition of the 3D simulations; (b) rendering of the initial condition of 3D simulations, the borders of the figure are the same as the yellow box in the upper panel (run F3f1.00c).
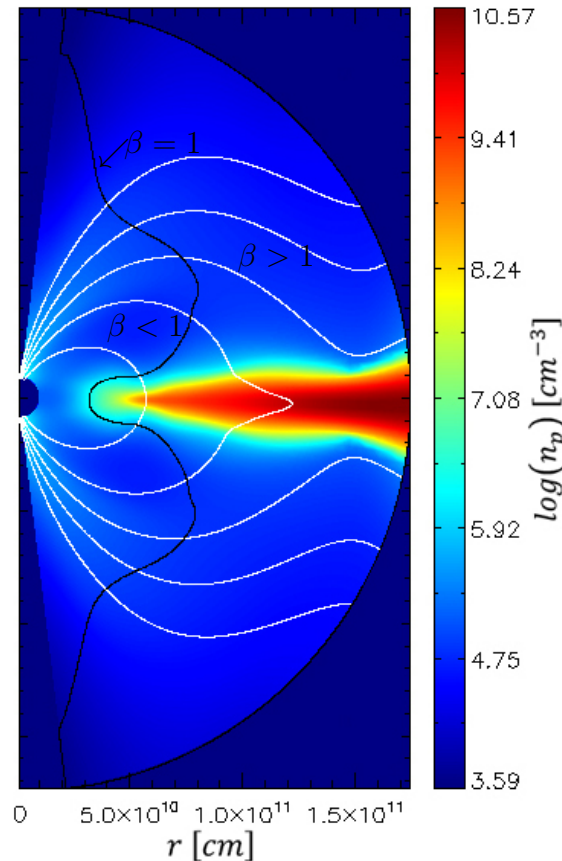
Figure 2.4: Colour-coded log scale of density distribution in a slice of the computational domain used as initial condition in the 3D simulation (see Fig. 2.3b). White lines represent the magnetic field lines projected in the $[r, \theta]$ plane, whilst the black line is the $\beta = 1$ surface with the $\beta < 1$ region on the left (run F3f1.00c).

As a second phase, we then use such a virtually relaxed and steady state as the initial conditions for our project. To this end we map the output of the 2.5D MHD simulations (namely the fully developed physical quantities: mass density, temperature, velocity and magnetic field), performed in the first phase, into a 3D domain in order to provide the initial condition of a 3D model describing the further evolution of the star-disk system (see Fig. 2.3). Due to the fact that the 2.5D domain covers only a slice of half hemisphere of the system, the 2.5D-into-3D mapping has been performed through a preliminary reflection across the equatorial plane followed by a rigid rotation about the z axis. Note that the 2.5D domain has been selected in order to describe in 3D only the inner part of it, where flaring activity is expected to occur, thus reducing the computational cost. Moreover, no phenomena relevant for the present study involve the external region of the disk. In the initial configuration of the 3D simulations (see Fig. 2.3b and 2.4) the magnetic field lines appear still in a dipole-like form. This is particularly evident in the corona closer to the star (i.e. the magnetosphere), where $\beta < 1$ and the region is field-dominated. On the other hand, in the external corona and, especially, inside the disk, where $\beta > 1$, the dynamics is matter-

dominated and the differential rotation of the plasma induces a noticeable deformation of the field lines. The 3D computational domain obtained in this way is defined in spherical coordinates (r, θ, ϕ) and consists of a computational cube of 128^3 cells. The radial direction has been discretized on a grid with interval size exponentially increasing with R. The domain extends from $R_{min} = 15R_*(\approx 9 \cdot 10^9 cm)$ to $R_{max} = 300R_*(\approx 1.8 \cdot 10^{11} cm)$. The radial grid is made of $n_r = 128$ points with a maximum resolution of $\Delta R = 2.1 \cdot 10^8 cm$, close to the star, and $\Delta R = 4.2 \cdot 10^9 cm$, close to the external part of the disk. The boundary conditions at R_{min} and R_{max} are the same as those used in the 2.5D runs. As for the angular coordinate θ, the computational domain spans an angle from $\sim 7°$ to $\sim 173°$, leaving two cones above star poles as not modelled. Hence, the boundaries in θ do not coincide with the rotational axis of the star-disk system in order to avoid extremely small $\delta\phi$ values cause strongly increasing computational cost. Moreover, all events relevant for the present study do not involve any region close to the rotation axis. The angular coordinate θ has been discretized uniformly using $n_\theta = 128$ points, giving a resolution of $\Delta\theta \sim 1.3°$. Zero-gradient boundary conditions are assumed for θ at $\sim 7°$ and $\sim 173°$. Finally, in the angular coordinate ϕ, the computational domain spans the angle from $\sim 0°$ to $\sim 180°$, with an uniform resolution of $\Delta\phi \sim 1.4°$. Thus the computational domain covers only half of the star-disk system. The boundary conditions for the coordinate ϕ are assumed to be periodic.

2.4   The PLUTO code

The calculation were performed using PLUTO (Mignone et al., 2007), a modular Godunov-type code (see Appendix C) developed mainly for astrophysical plasmas involving high Mach number flows in multiple spatial dimensions. The code embeds different physics modules (allowing the treatment of hydrodynamics and magneto-hydrodynamics both relativistic and non-relativistic in Cartesian or curvilinear coordinates) and multiple algorithms particularly oriented toward the treatment of astrophysical flows in the presence of discontinuities. These features make PLUTO a flexible and versatile modular computational framework to solve the equations describing astrophysical plasma flows. PLUTO is entirely written in the C programming language and was designed to make efficient use of massive parallel computers using the message-passing interface (MPI) library for interprocessor communications. The MHD equations are solved using the available MHD module, configured to compute inter-cell fluxes with the Harten-Lax-Van Leer (HLL) approximate Riemann solver. In order to solve the equation vs. time, we used a second order Runge-Kutta (RK) integration scheme (see Appendix C). Moreover, a minmod limiter for the primitive variables has been used, in order to avoid spurious oscillations that could otherwise occur due
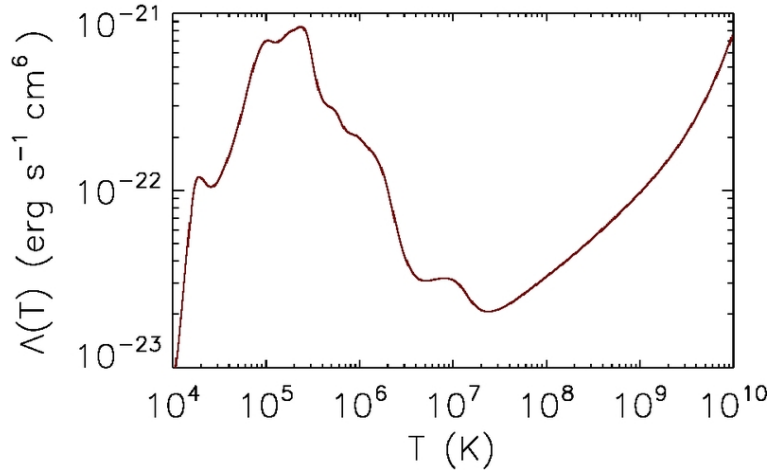
Figure 2.5: The radiative losses per unit emission measure $\Lambda(T)$ as a function of temperature.

to shocks, discontinuities or sharp changes in the solution domain. As for magnetic field, its evolution is computed adopting the constrained transport approach (Balsara & Spicer, 1999) that maintains the solenoidal condition ($\nabla \cdot B = 0$) at machine accuracy. Moreover, we adopted the *magnetic field-splitting* technique (Tanaka, 1994; Powell et al., 1999; Zanni & Ferreira, 2009) by splitting the total magnetic field into a contribution coming from the background stellar magnetic field and a perturbation to this initial field. Then only the latter component is computed numerically. This approach is particularly useful when dealing with low-β plasma as it is the case in proximity of the stellar surface (Zanni & Ferreira, 2009). PLUTO takes into account radiative losses from optically thin plasma. The radiative losses are computed as

$$\Lambda = n^2 \Lambda(T_i) \qquad \text{with} \qquad n = \frac{\rho}{\mu m_H} \tag{2.22}$$

at the temperature of interest, using a lookup-table/interpolation method, where $\Lambda_i = \Lambda(T_i)$ is available along with T_i as a sampling at discrete point (see Fig. 2.5). The lookup table used has been generated with *Cloudy 90.01* for an optically thin plasma and solar abundances (thanks to T. Plewa). *Cloudy* models the ionization, chemical, and thermal state of material that may be exposed to a external radiation field or other source of heating, and predicts observables such as emission and absorption spectra from hard X-rays to the radio regime. The 30 lightest elements, from hydrogen to zinc, are included, and the solver balances radiative and collisional ionization and recombination (Ferland et al., 1998, 2013; Salz et al., 2015). The thermal conduction as well the viscosity is treated separately from advection terms through operator splitting. In particular we adopted the super-time-stepping technique (Alexiades et al., 1996) which has been proved to be very

effective to speed up explicit time-stepping schemes for parabolic problems. This approach is crucial when high values of plasma temperature are reached (as during flares), explicit scheme being subject to a rather restrictive stability condition (i.e. $\Delta t < (\Delta x)^2/(2\eta)$, where η is the maximum diffusion coefficient), as the thermal conduction timescale τ_{cond} is typically shorter than the dynamical one τ_{dyn} (Hujeirat & Camenzind, 2000; Hujeirat, 2005; Orlando et al., 2005, 2008).

The code has been developed at the Turin Astronomical Observatory in collaboration with the Department of General Physics of the Turin University and it is freely available at http://plutocode.ph.unito.it under the GNU general public license.

2.5   Synthesis of the thermal X-ray emission

From the model results we synthesize the thermal X-ray emission originating from the disk-corona system in different spectral bands of interest: $[0.1-2.0]\ keV$ and $[2.0-10.0]\ keV$. We apply a methodology analogous to the one described by Orlando et al. (2009). The results of numerical simulations are the evolution of the various physical quantities of interest (density, temperature, velocity and magnetic field) of the plasma in half of the spatial domain. In order to get full emitted radiation, we reconstruct the 3D spatial distribution of these physical quantities in the whole spatial domain. We rotate the system around the x axis to explore different inclinations of the orbital plane relative to the sky plane. From the value of temperature and emission measure of the i-th computational cell we synthesize the corresponding thermal X-ray emission, using the Astrophysical Plasma Emission Code (APEC) (Smith et al., 2001) of hot collisionally ionized plasma. APEC models provide emissivity tables of both line and continuum emission which may be used to calculate predicted fluxes. These predicted fluxes may, in turn, be compared with observed spectral features. The predicted flux is given by:

$$F = \frac{\epsilon(T)}{4\pi R^2} \int n_e n_H dV \quad \Rightarrow \quad F_i = \frac{\epsilon(T_i)}{4\pi R_i^2} n_i^2 V_i, \tag{2.23}$$

where $\epsilon(T)$ is the emissivity in $erg\ cm^3/s$, R is the distance to the source in cm, and the integral is the emission measure in cm^{-3}. Therefore, defining i as the index of a cell of the computational domain, $\epsilon(T_i)$ is the emissivity of the cell at temperature T_i, whilst emission measure is defined as $EM_i = n_i^2 V_i$, where n_i is the proton number density in the cell and V_i is the volume of the cell where plasma is assumed to be fully ionized. The spectral synthesis takes into account the Doppler shift of emission lines due to the plasma velocity component along the line of sight (LoS). We assume solar metal abundances of Anders & Grevesse (1989) for the circumstellar medium (CSM). The X-ray spectrum emitted by each

computational cell is filtered through the CSM absorption column, going from the cell to the observer along the LoS. The CSM absorption is computed using the absorption cross-section as a function of wavelength from Balucinska-Church & McCammon (1992). The thermal X-ray emission, integrated along the LoS in the whole computational domain, defines an image describing the distribution of X-ray flux; the flux values are computed assuming a distance of 500 pc and no interstellar absorption. Then, through the integration of the fluxes of the images, we obtain the total emission at the selected time; the sequence of all these values at different times yields the lightcurve in the selected energy bands.

Chapter 3

Results

3.1 Explored system configurations

The model described in Chapter 2 allows to explore different configurations of the system changing some main input parameters. In fact, once we set the truncation radius at $R_d = 45R_*$, where the β of plasma is imposed equal to unity, we can change the value of density at the surface of the disk and, consequently, obtain the surface magnetic field of the white dwarf needed to keep $\beta = 1$ at the truncation radius R_d. The various configurations of the system taken into account have been chosen in order to have a sampling as wide as possible of magnetic field strength found in this kind of systems, that ranges between 0.1 and 10 MG. We take as a reference model the one defined as F4f1.00a in Table 3.1, in which the surface magnetic field intensity is ≈ 5 MG. Other parameters have been taken into account in our exploration of the parameter space. In particular we explored the maximum intensity of the flares and their frequency as well. Table 3.1 summarises the various simulations and details main parameters characteristic of each run: ρ_c and ρ_d are, respectively, coronal density and disk density at the layer between corona and disk; T_c is the initial uniform temperature of the corona; n_d is the maximum density of particles in the bulk of the disk; B_{sup} is the magnetic field intensity at the surface of the star; FF is the frequency of flare release, and finally I_{max} is the maximum energy release of the flares.

3.2 System dynamics

For our reference case, F4f1.00a, the energy release of the intense flaring activity has been followed for approximately 20 minutes. Each heat pulse triggers a MHD shock wave that develops above the disk, preferentially propagating away from the central star, in the region where $\beta > 1$. The abrupt release of energy determines a local increase of temperature and pressure, heating the dense plasma of the disk. While each flare develops, the heat

Table 3.1: Main input parameters defining initial condition described in Section 2.2.

Run	ρ_d $[g/cm^3]$	ρ_d $[g/cm^3]$	T_c $[K]$	n_d $[cm^{-3}]$	B_{sup} $[G]$	FF $[s^{-1}]$	I_{max} $[erg\ cm^{-3}s^{-1}]$
F3f1.00c	$1.0\ 10^{-19}$	$2.0\ 10^{-17}$	10^7	$1.8\ 10^{10}$	$1.6\ 10^5$	$1/5$	10^{34}
F6f1.00a	$1.0\ 10^{-17}$	$2.0\ 10^{-15}$	10^7	$1.8\ 10^{12}$	$1.6\ 10^6$	$1/5$	10^{34}
F4f1.00a	$1.0\ 10^{-16}$	$2.0\ 10^{-14}$	10^7	$1.8\ 10^{13}$	$5.0\ 10^6$	$1/5$	10^{34}
F4f1.00e	$1.0\ 10^{-16}$	$2.0\ 10^{-14}$	10^7	$1.8\ 10^{13}$	$5.0\ 10^6$	$1/10$	10^{34}
F4f0.01f	$1.0\ 10^{-16}$	$2.0\ 10^{-14}$	10^7	$1.8\ 10^{13}$	$5.0\ 10^6$	$1/2.5$	10^{32}
F4f1.00f	$1.0\ 10^{-16}$	$2.0\ 10^{-14}$	10^7	$1.8\ 10^{13}$	$5.0\ 10^6$	$1/2.5$	10^{34}
F4f1.00g	$1.0\ 10^{-16}$	$2.0\ 10^{-14}$	10^7	$1.8\ 10^{13}$	$5.0\ 10^6$	$1/100$	10^{34}
F4f10.0g	$1.0\ 10^{-16}$	$2.0\ 10^{-14}$	10^7	$1.8\ 10^{13}$	$5.0\ 10^6$	$1/100$	10^{36}
F5f1.00a	$4.0\ 10^{-16}$	$8.0\ 10^{-14}$	10^7	$7.1\ 10^{13}$	$1.0\ 10^7$	$1/5$	10^{34}

Coronal density ρ_c and disk density ρ_d refer to the values at the layer between corona and disk. The density of particles n_d is the maximum density in the bulk of the disk. FF is the frequency of flare release.
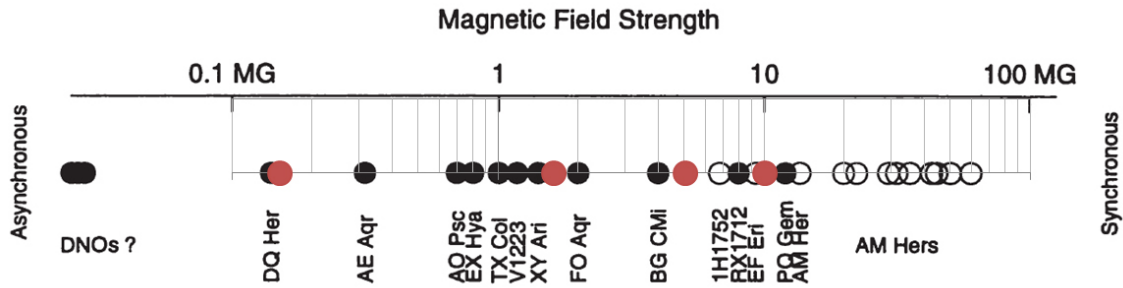

Figure 3.1: Distribution of magnetic field strengths for *MCVs*: *PCVs* (open circles) and *IPCVs* (filled circles) form an overlapping continuum (Dhillon, 1996; Seward & Charles, 2010). Red dots represent the intensity of magnetic field taken into account in the simulations.

pulse determines an overpressure in the region of the disk corresponding to the footpoint of the loop. This overpressure travels as a pressure wave through the bulk of the disk, eventually reaching the opposite surface of the disk. The heated disk material expands in the magnetosphere propagating above the disk with a strong evaporation front moving at speed of the order of $10^8\ cm/s$. The heated and expanding plasma interacts with magnetic field, with mutual effects. As a matter of fact, during the evolution of the system, the field lines, in regions where β has high values, are dragged away and slowly deformed by the action of the flares, and, eventually, only the magnetosphere close to the star keeps an approximately dipolar shape. Analogously, the hot evaporation front triggered by each flare is strongly affected by the interaction with the magnetosphere, and, where $\beta < 1$, the hot plasma is channelled along the magnetic field lines toward the central white dwarf. A few minutes after each energy release, a hot ($T \sim 10^9 K$) magnetic loop of length of the order of $10^{10} cm$ is formed, linking the disk with the star. The loop continues to expand for almost

8 minutes, and the temperature decreases by almost 2 orders of magnitude. The frames in Fig. 3.2 show the evolution of density, pressure and temperature distribution of two successive flares in a slice of the domain perpendicular to the equatorial plane and aligned with the symmetry axis. The first flare occurs in a low β region closer to the star, whereas the second one occurs in a high β region. Both flares are triggered at approximately the same angle ϕ. For the first flare, the magnetic field, due to a low β, produces the channelling of the hot plasma, forming a magnetic loop linking the star and disk, while the the second one appears as not magnetically confined. The plasma starts cooling as soon as the heat deposition is over, as a result of the combined action of the efficient radiative cooling and thermal conduction. In particular, on one hand, thermal conduction from the outer layer of hot plasma sustains the disk evaporation that goes on even after the flare decays. On the other hand, thermal conduction, due to its high anisotropy in presence of the magnetic field (see Eq. 2.9), promotes the development of a hot magnetic tube (loop) linking star and disk, through the formation of a fast thermal front propagating along the magnetic field lines toward the star and reaching it in a time-scale of $\approx 1\,min$ (lower panels of Fig. 3.2).

During the system evolution, the combined effect of the storm of flares causes the formation of an extended corona between disk and star (see panels in Fig. 3.3). Nevertheless, most of the evaporated disk material, particularly in the external regions of the disk, is not completely confined by magnetic field and is not efficiently channelled into the loops but it escapes upward and is ejected away in the outer regions, carrying away mass and angular momentum.

3.2.1 Effect of density and magnetic field intensity

The main difference between the various models explored lies in the density of the circumstellar atmosphere and consequently in the magnetic field intensity, while we keep the energy released by flares the same. Due mainly to a denser disk, the effects of the pressure wave moving across the disk caused by each flare are mild in configurations with denser disk and stronger magnetic field (i.e. runs F4f1.00a and F5f1.00a, see bottom panels in Fig. 3.4). In these two cases, the perturbation of the disk is limited to the surface of the disk and the field lines are slowly deformed by the action of the MHD shock. On the other hand, the flares cause a perturbation that is more evident in low density/weak field configurations (i.e. runs F3f1.00c and F6f1.00a, see top panels in Fig. 3.4). Moreover, in these configurations, the perturbation of the disk causes a fast and evident deformation of the field lines. So, due to a less dense disk, the flaring activity can strongly alter the configuration of the disk potentially hampering its overall stability, possibly triggering accretion phenomena. In Fig. 3.5 the effect of flaring activity in a low density/weak field configuration (i.e. F6f1.00b)
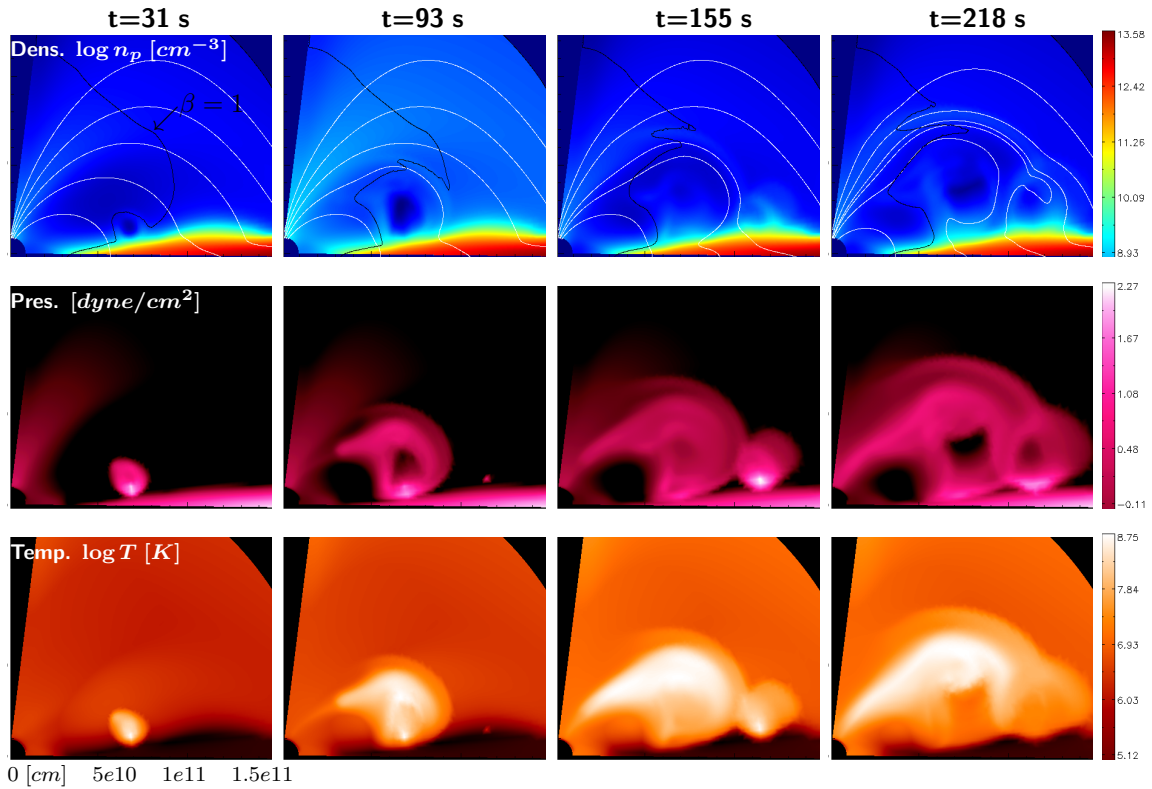
Figure 3.2: Two following flaring loops during their evolution. The figure shows the distribution of density (upper panels), pressure (middle panels) and temperature (lower panels) in a slice in the $[r, \theta]$ plane passing through the middle of the loops. In the upper panels white lines represent magnetic field lines projected in the $[r, \theta]$ plane, while black line shows the $\beta = 1$ surface. The slice encompasses an angular sector going from the rotation axis to the disk equatorial plane. The first flare occurs in a $\beta < 1$ region and produces a magnetically confined loop linking star and disk, the second flare is released in a $\beta > 1$ region at approximately the same angle ϕ, and the hot plasma is not magnetically confined (run F4f1.00a).

is shown: the disk surface is visibly perturbed and plasma is channelled by the magnetic field in the magnetosphere close to the star, developing funnel flows.

3.2.2   Effect of flare frequency and intensity

Another important element differentiating the various models is how often and how intense is the energy release associated to each flare. As expected, frequency and intensity of the flares have remarkable effects on the disk and on the magnetic field lines. In fact, a higher flare frequency or a more intense energy release, produces a noticeable disk disruption along with a deeper dislocation of the magnetic field lines, compared to analogous models characterized by a less intense and less frequent flaring activity.
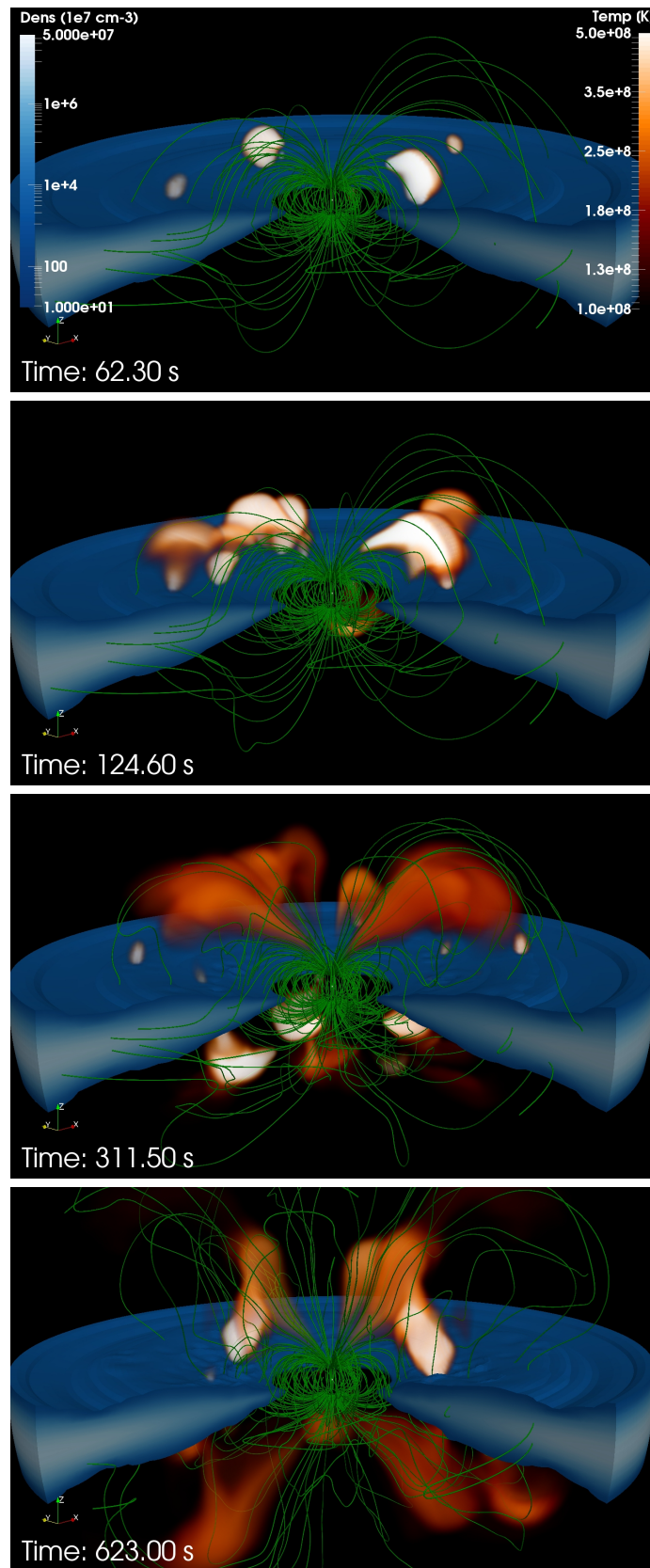
Figure 3.3: Effect of a hail of flares on the disk and on the circumstellar atmosphere. The cutaway views of the star-disk system show the mass density (blue) and the magnetic field lines (green) at different times. The 3D volume rendering of the plasma temperature is over-plotted, showing the flaring loops (red-yellow) linking the inner part of the disk with the central white dwarf (run F4f1.00a).
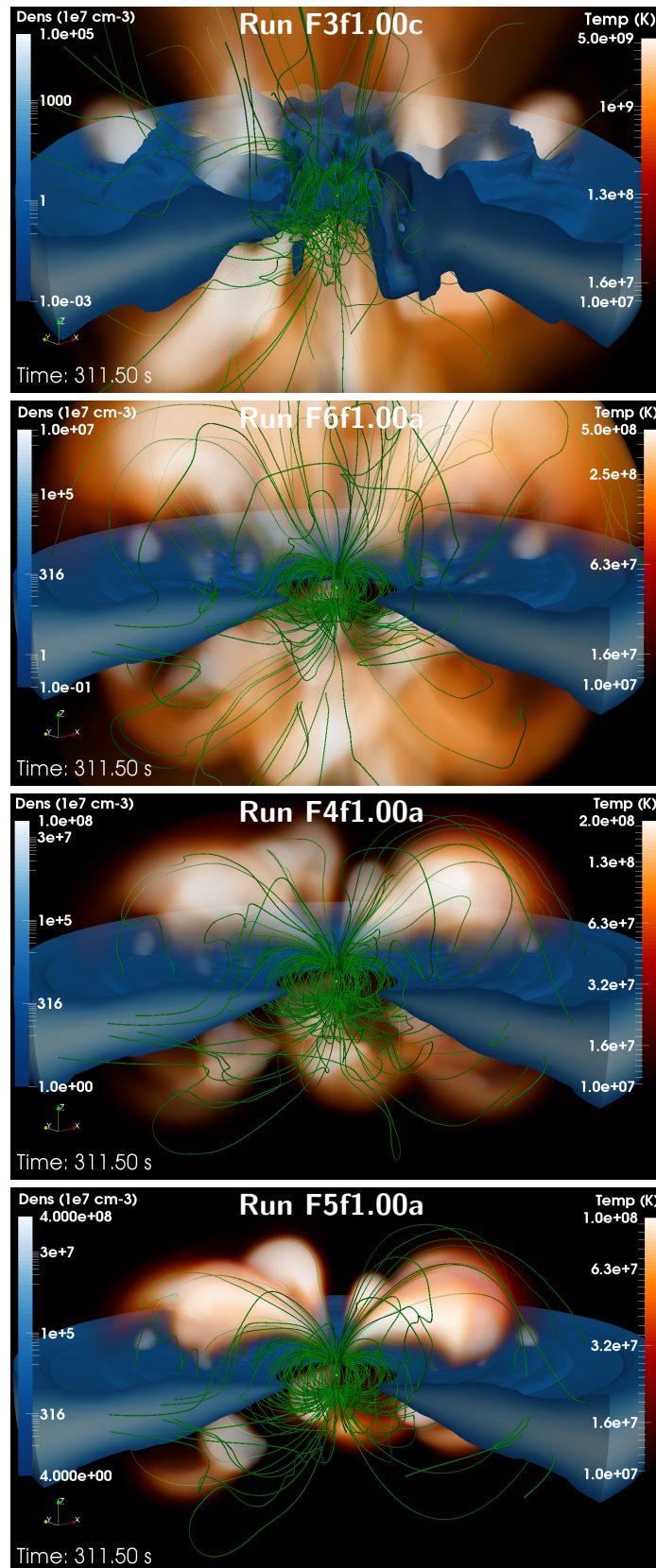
Figure 3.4: The above images represent the different effects of the same energy release at the same time ($t = 311.50$ s) on different configurations of the system with progressively denser disks and stronger magnetic field, from top to bottom. The cutaway views of the star-disk system show the mass density (blue) and the magnetic field lines (green). The 3D volume rendering of the plasma temperature is over-plotted, showing the flaring loops (red-yellow).
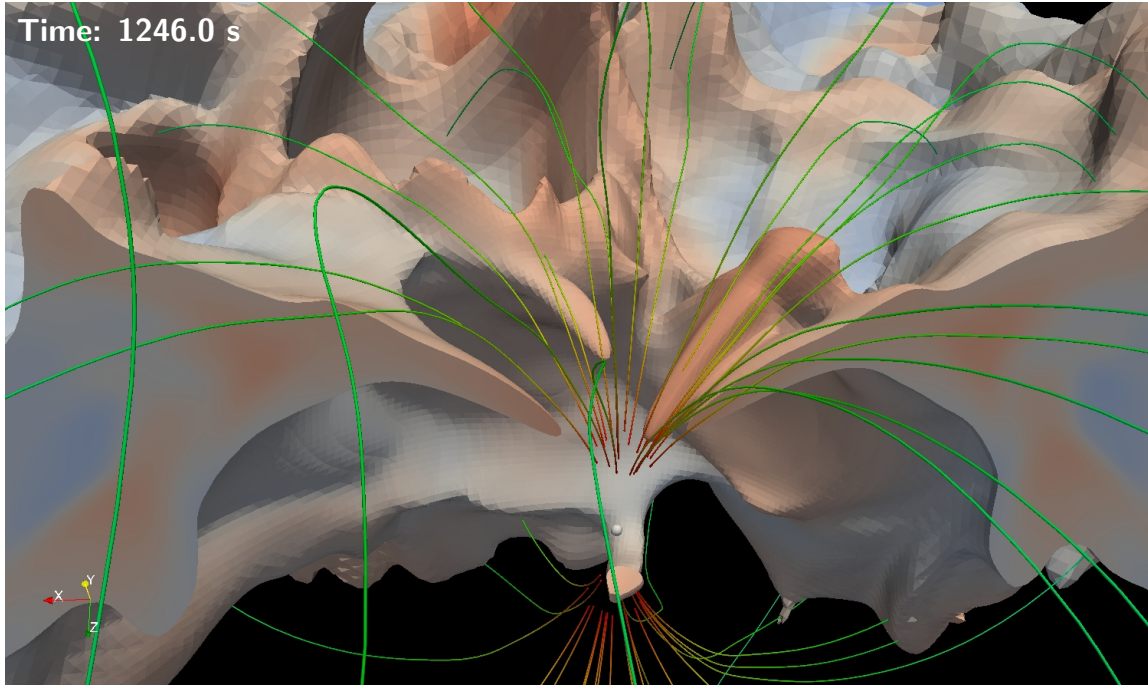
Figure 3.5: Accretion streams triggered by the strong perturbation of the stability of the accretion disk, that before the start of the flares was in the equatorial plane. The system here considered is in a low density/low field configuration (run F6f1.00a). The little white sphere represents the white dwarf ($R_{wd} = 6 \cdot 10^8$ *cm*), whilst green lines are magnetic field lines.

3.2.3   Effect of flaring activity on accretion

We also analysed the effect of the flaring activity on the accretion. Fig. 3.6 shows the mass accretion rate during the evolution of the system subject to the storm of flares in the several models explored. It is worth noting that the value of accretion in all the configurations taken into account is below the expected value of mass accretion rate theoretically determined for the whole class of *IPCV*s, that usually ranges between 10^{-11} and 10^{-8} $M_\odot y^{-1}$ (Patterson, 1984, 1994; Giovannelli et al., 2012). This behaviour could be in accordance with the theory of magnetic compact stars accreting from a disk, developed by Ghosh & Lamb (1978). According to these studies, the accretion should be highly inhibited for short-period systems, due to a spin equilibrium determined by the spin-up torque exerted on the disk by the magnetic field lines. In our model we are actually taking into account a fast rotator ($T_{spin} \cong 5.4$ *min*), for which the "fastness parameter" $\omega_s = \omega_*/\omega_d = 1$, where ω_d is the angular velocity at the magnetospheric radius (i.e. the truncation radius R_d). According to this theory, when ω_s is greater than the critical value of ω_s ($\equiv \omega_{crit} = 0.35 - 0.85$), accretion should be stopped or highly inhibited. Moreover, due to the strong perturbation induced by flares, in the lowest field configuration (run F3f1.00c, Fig. 3.6) the accretion rate caused by flares is highly influenced by the flaring activity. In fact, unlike the other
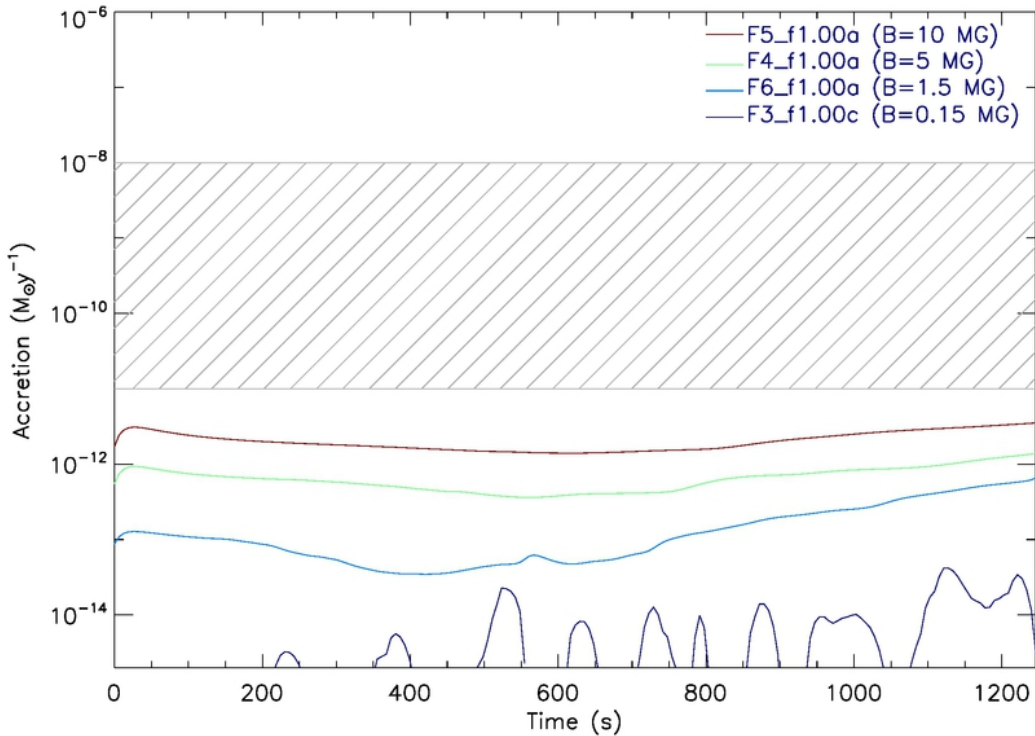
Figure 3.6: Mass accretion rate during the evolution of the system subject to the intense flaring activity in the several models analysed. The shaded area corresponds to the expected accretion rate from the theory of a radially accreting white dwarf (Patterson, 1984, 1994; Giovannelli et al., 2012).

configurations, there is no steady inflow from the disk, rather an irregular stream appears. In this configuration the energy released by flares can strongly influence the field even in the inner magnetosphere, affecting the magnetic channelling of plasma in this region.

3.3   Thermal X-ray emission

Since we are interested in investigating the thermal X-ray emission originating from the activity occurring on the surface of the disk, finally, we analysed the emission measure (see Section 2.5) of the plasma at temperature capable of producing thermal X-ray emission $(T > 10^6 K)$. Fig. 3.7 shows that immediately after the beginning of the release of heat pulses, the amount of plasma at temperature greater than 1 MK, increases steadily reaching an almost steady-state condition after 100 seconds. The values of emission measure found indicate that the flaring activity leads to a strong thermal X-ray emission.

From the model results, we synthesized the thermal X-ray emission originating from the whole system along the whole interval of time considered in our simulations. The methodology applied is described in Section 2.5. The thermal X-ray emission has been synthesized in two bands: the soft ($[0.1 - 2.0]$ keV) and the hard ($[2.0 - 10]$ keV). Fig. 3.8 represents
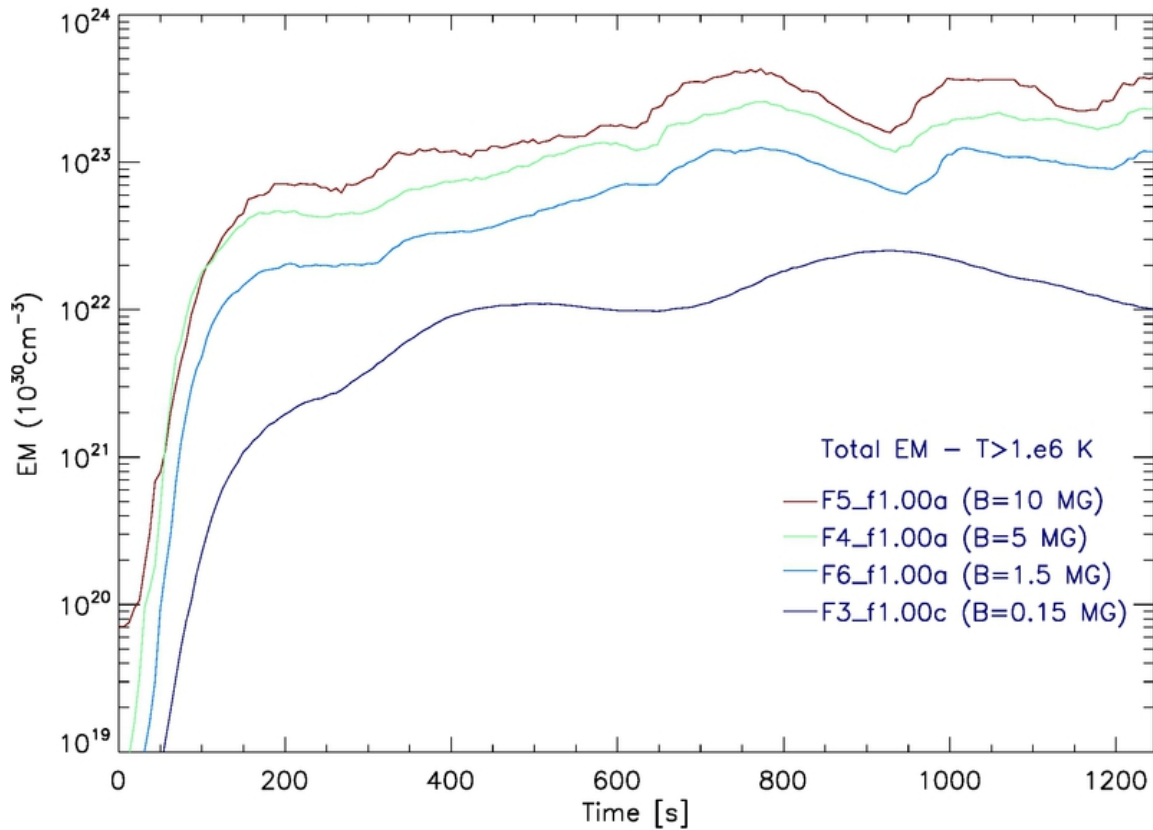
Figure 3.7: Total emission measure vs. time of plasma hotter than 1 MK. After few minutes, the value of emission measure approaches a virtually steady-state condition (run F4f1.00a).

some of the synthesized X-ray images. Each image shows the simulated spatial distribution of thermal X-ray flux observed at different times during the evolution of the system. The system is observed from a line of sight forming a 45° angle with the equatorial plane. From these X-ray images we can infer where the coronal emission is more conspicuous. We identify the feet of the coronal loops as the regions where the thermal X-ray emission is concentrated. On the whole, the flaring activity seems to be capable of triggering the formation of a hot and tenuous layer of plasma extending on the disk surface. This layer is accountable for the bulk of thermal X-ray emission, that is concentrated in proximity of the disk surface.

3.3.1   Effect of density and magnetic field intensity

The flux values of the thermal X-ray emission have been used in order to obtain the lightcurves for each model. The fluxes are defined as the total energy per unit of surface and per unit of time and the corresponding luminosity is obtained from these fluxes supposed to be measured at a distance of 500 pc. Fig. 3.9 shows the comparison between the lightcurves of the various configuration investigated with a frequency of a flare every
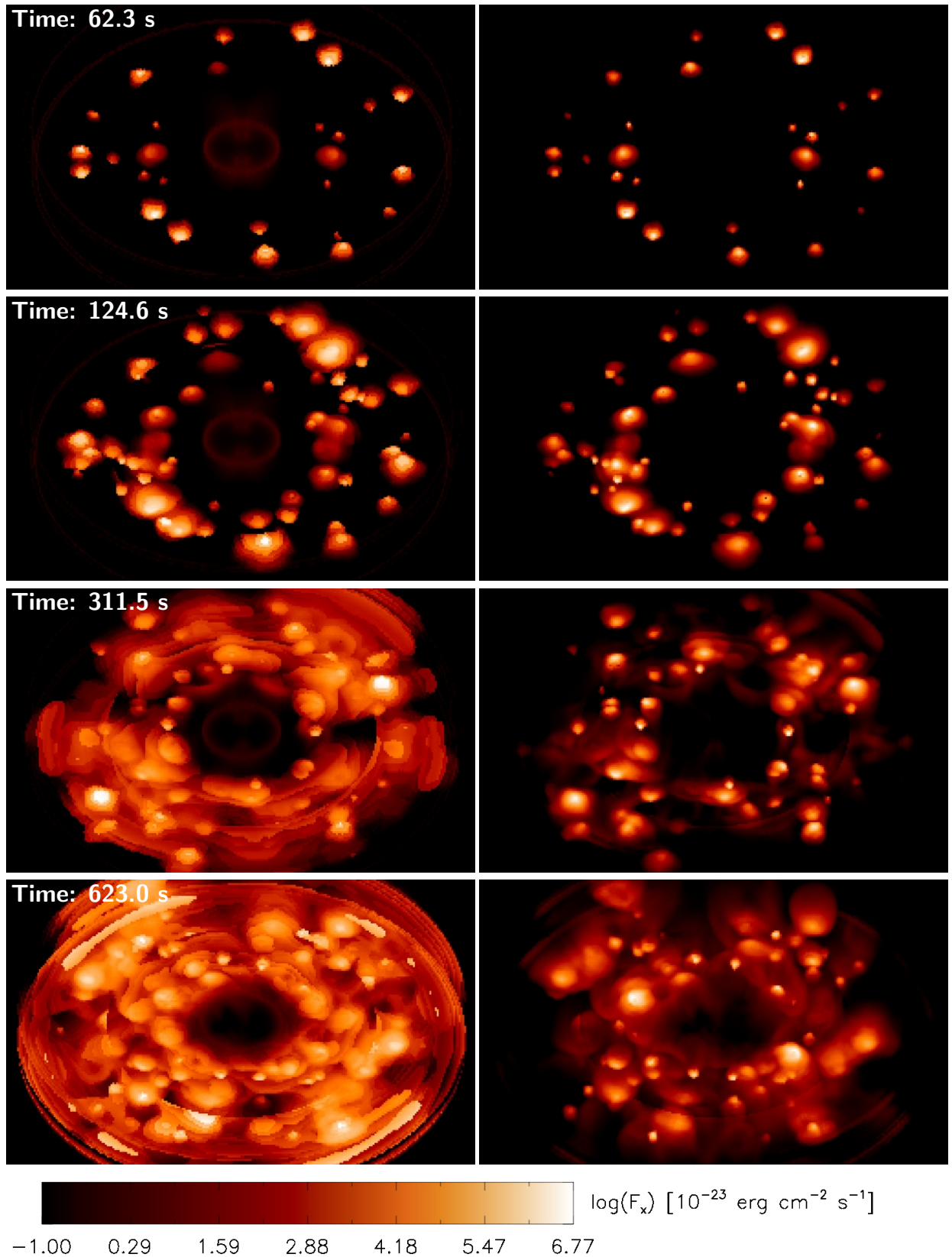
Figure 3.8: X-ray images of the whole domain as seen by an observer with a line of sight of 45° with the equatorial plane. On the left column panels soft X-ray $[0.1 - 2.0]$ keV fluxes, on the right hand side panels hard X-ray $[2.0 - 10]$ keV fluxes, as they would be measured by an observer at 500 pc. The images refers to the run F4f1.00a and are taken at the same time-steps of Fig. 3.3 and ordered vertically.

5 seconds (assumed as reference value). The luminosity, in every configuration explored, reaches in few minutes the quasi-stationary condition and exhibits a clear oscillation. This effect is actually less noticeable in low field configurations (i.e. runs F3f1.00c and F6f1.00a) because these configurations are characterized by low density values. The density, through the term n^2 (see equation (2.3)), strongly affects the radiative cooling. So, in low density configurations, the energy injected by each heat pulse is more slowly dissipated than in high density ones, and, when another pulse is released, the effect of the energy injected by the previous one has not been dissipated yet. In this case the effect of each flare is less evident in the global light curve.

Another key element, that we can infer from the lightcurves, is the maximum luminosity achieved: the denser is the disk and, consequently, the stronger the magnetic field, the higher is the luminosity. In fact, a denser plasma determines a higher value of emission measure, hence the contribution to the emission is greater. Comparing the lightcurves of the harder band with the corresponding ones of the softer band, we find a hardness ratio of the spectra, namely the ratio between hard and soft X-ray luminosity, approximately $\lesssim 0.1$.

3.3.2   Effect of flare frequency and intensity

In the context of the reference model we also explored the effect of the frequency and intensity of flares on the lightcurves. Fig. 3.10 shows how the lightcurves are affected by different flare release frequencies. The difference between maximum and mean value ranges between a factor of 5 and 8 of the mean value in high flare frequency configurations (run F4f1.00f, F4f1.00a and F4f10.00e), whilst, in low flare frequency ones (run F4f1.00g and F4f10.00g), this value rises up to 57 times the mean value. From this comparison, we can infer that the variability of thermal X-ray emission strongly depends on the rate of triggered flares. Actually, as long as the period between two subsequent flares is shorter than the duration of each energy pulse ($100s$), the variability of the luminosity value is less noticeable and the effect of each single flare is mixed and superimposed to the ones of the other neighbour flares. We actually observe a background emission due to many small flares evolving simultaneously while higher peaks are due to the strongest flares. When the period between flares is the same of the duration of the energy pulse, the effect of each single pulse is easily identifiable. We can observe the fast rise and the subsequent slow decay of thermal X-ray emission characteristic of each flare. Indeed, for high temperature plasma the conductive and the radiative cooling are more effective (see Fig. 2.5), causing a quicker decrease of emission. This feature determines a noticeable modulation of luminosity as a sequence of partially overlapping bursts. Furthermore, the variability of the luminosity is
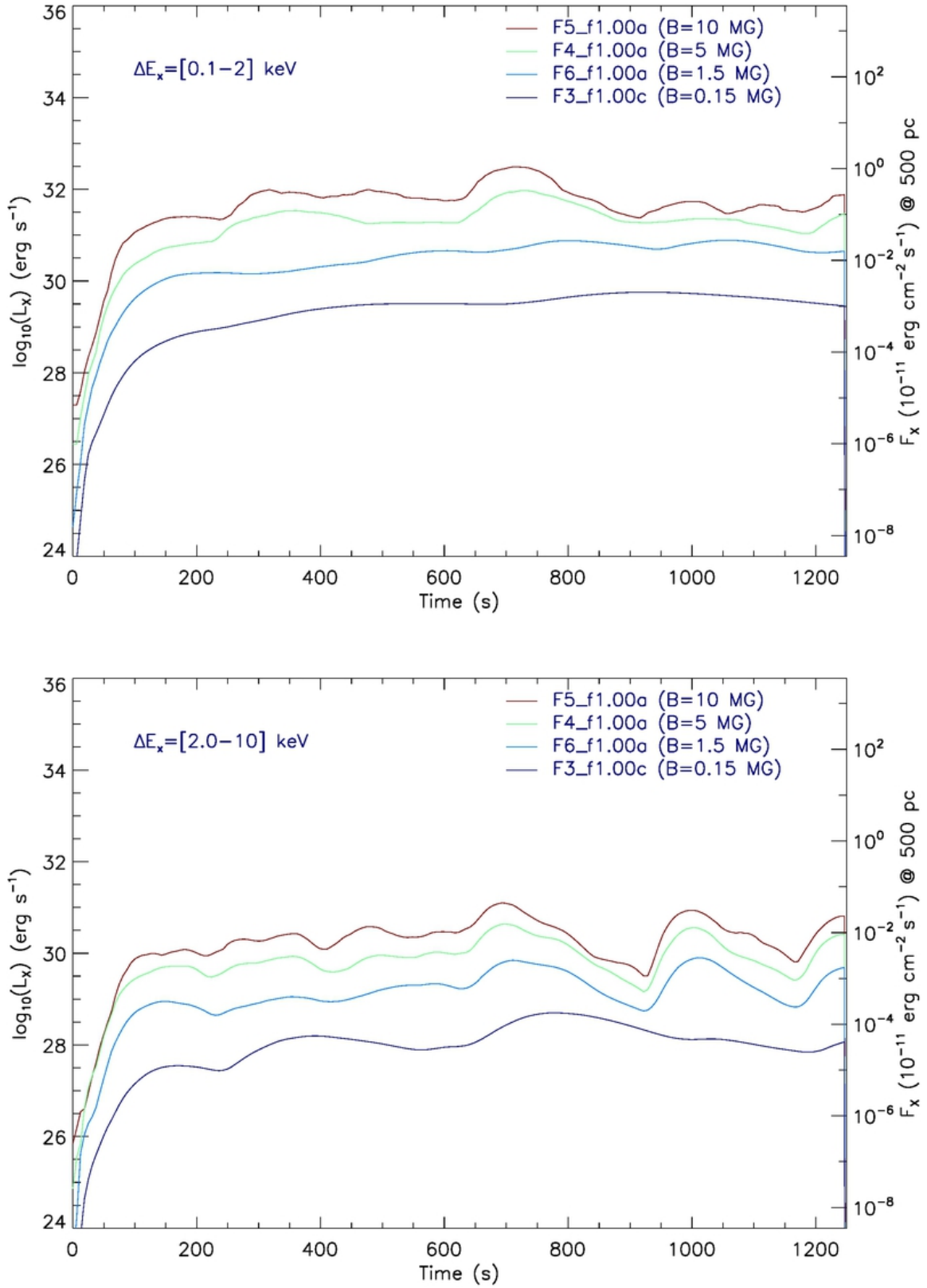
Figure 3.9: Comparative plot of lightcurves relative to various configurations explored for different values of magnetic field. On the upper panel, soft X-ray band $[0.1-2.0]$ keV lightcurves; on the lower panel, hard X-ray band $[2.0-10]$ keV lightcurves.
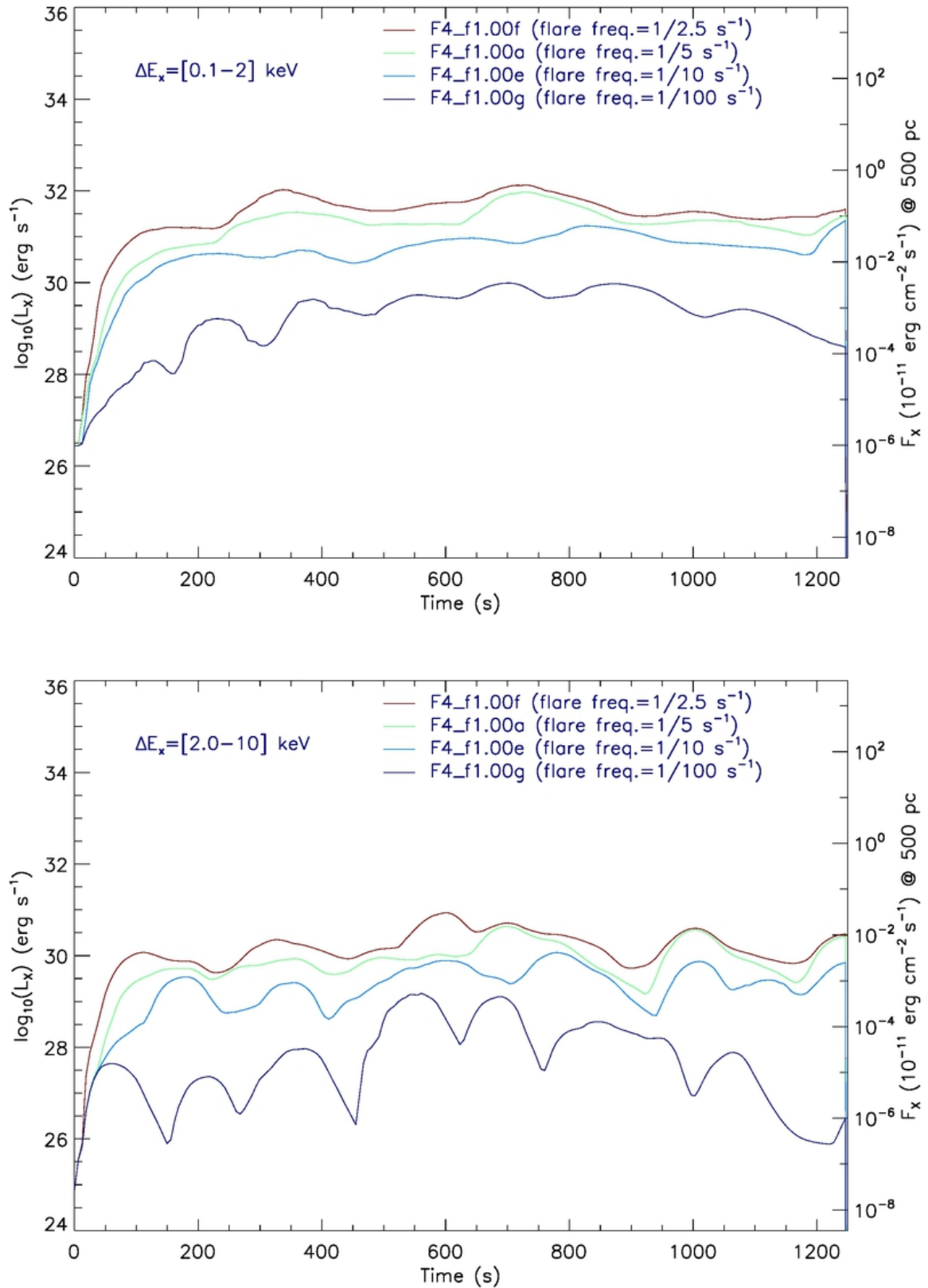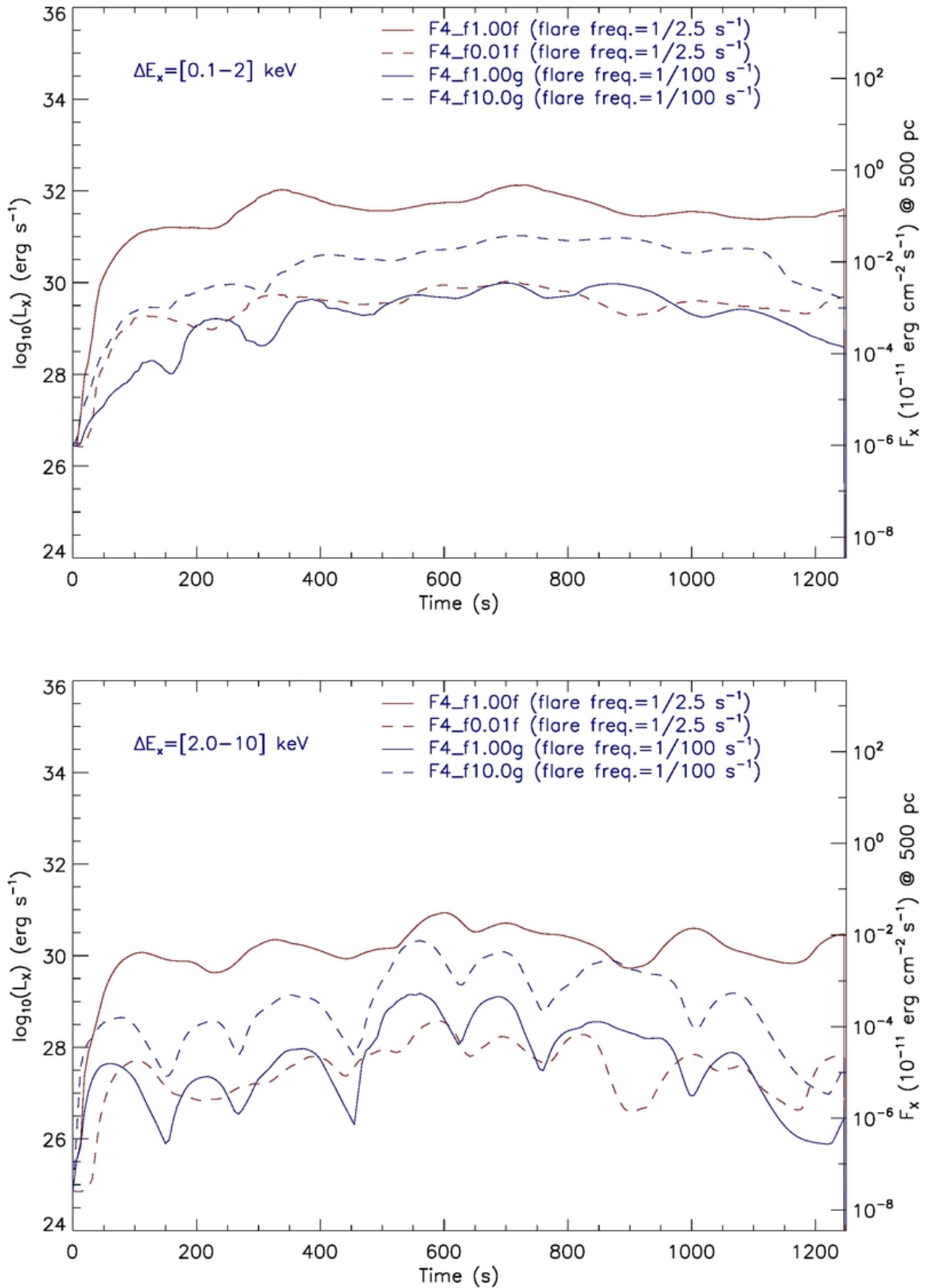
Figure 3.10: Comparative plot of lightcurves relative to the reference model. The explored parameter is the frequency of the energy pulse (flares). On the upper panel, soft X-ray band $[0.1 - 2.0]$ keV lightcurves; on the lower panel, hard X-ray band $[2.0 - 10]$ keV lightcurves.

Figure 3.11: Comparative plot of lightcurves relative to the reference model. The explored parameters are the frequency and the intensity of the energy pulse (flares). On the upper panel, soft X-ray band $[0.1 - 2.0]$ keV lightcurves; on the lower panel, hard X-ray band $[2.0 - 10]$ keV lightcurves.

generally more evident in the hard than in the soft band, because the hotter plasma is the dominant source of the hard emission.

Finally, Fig. 3.11 shows a comparison between lightcurves, taken in the context of the reference model with the same flare frequency but different maximum intensity. This comparison shows that the thermal X-ray variability strongly depends on the flare frequency, while the main effect of a higher intensity of flares is to bring up the average luminosity keeping, at the same time, the modulated shape almost unchanged.

3.4 Preliminary studies of disk stability

So far we have investigated the effects of a storm of flares occurring on the surface of the accretion disk of several *IPCV* system prototypes with different values of density and magnetic field intensity. We found out that this flaring activity can impact on the disk configuration and its structure, being able to efficaciously deform the magnetic field lines, with effects strongly dependent on density and magnetic field intensity.

Indeed, we have profoundly perturbed some system's configurations but we do not know if a strongly perturbed accretion disk can recover to a quiescent state, and to which extent it can be similar to the initial pre-flare one. In the light of that, we decided to proceed with our exploration of the dynamics of star-disk systems conducting a numerical experiment. To this end, we performed a series of simulations on the relaxation phase of the more strongly perturbed accretion disks among the models we explored in the present thesis. The main questions we would like to answer are: can a strongly perturbed accretion disk recover to a quiescent state, or is it disrupted beyond recovery? Under which conditions is it possible? How quickly?

In order to start this investigation, we chose the model F6f1.00a, i.e. a low density/low field configuration (see Table 3.1), and, once the heat release is over, we let the system evolve without any further external perturbation or transient heating. To date, the simulation has lasted for almost 60 minutes after the end of the flaring activity and it is still running. From the first outcomes of the system evolution we can infer that the relaxation process starts immediately after the shut-off of the heating. The disk, strongly perturbed by the flares, slowly expands and progressively levels off its surface, initially rough and overheated at about $5 \ 10^5 \ K$ (almost ten time higher than the initial temperature of the disk). During the first minutes following the end of the flaring activity accretion streams form, linking the inner part of the disk with the central star. The streams last for almost 15 minutes then they die out. The process of expansion and smoothing of the initially choppy surface continues and at the last step of the simulation the disk is noticeably swollen and the surface visibly smoothed. Fig. 3.12 and Fig. 3.13 show the system at some times during its
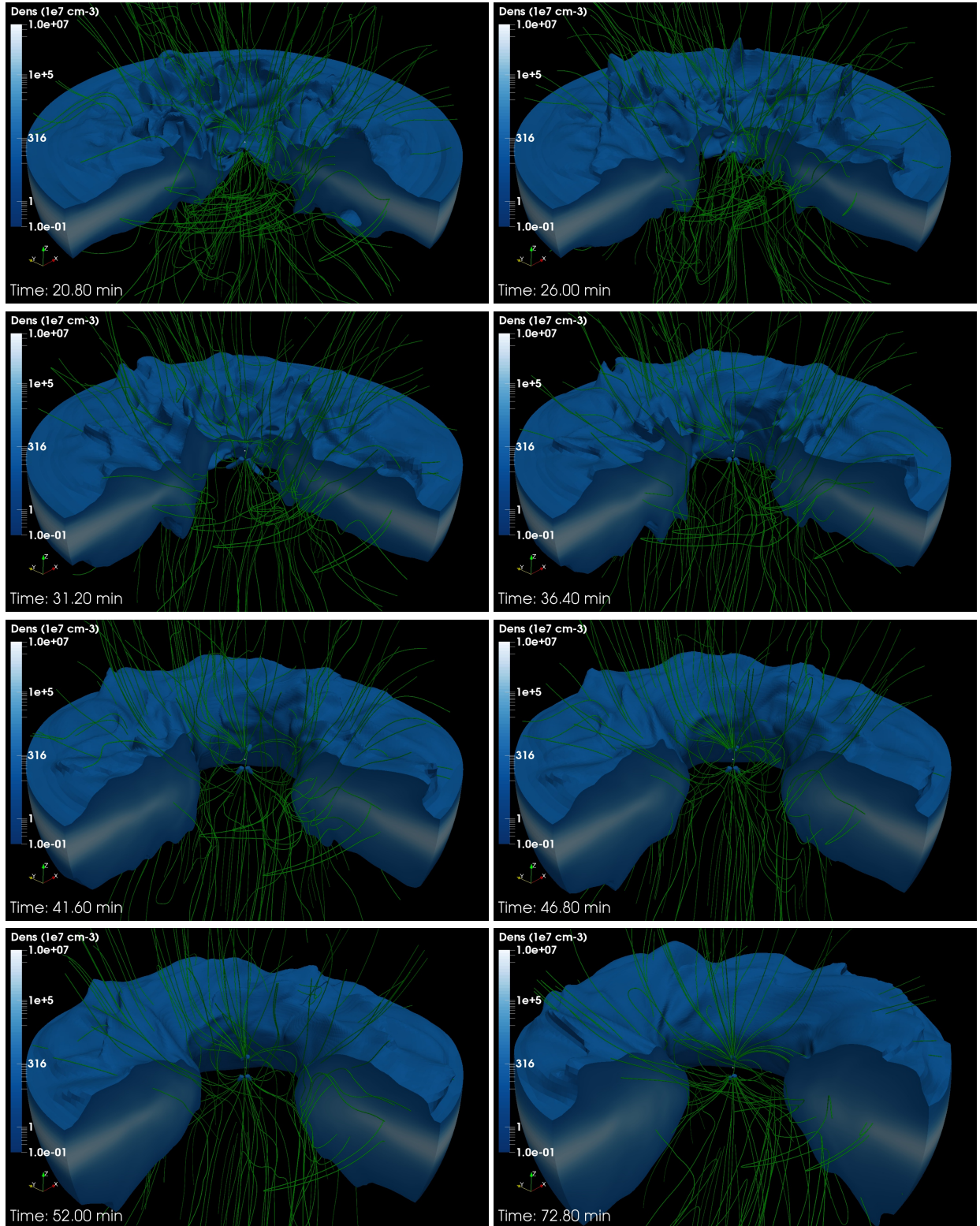
Figure 3.12: The above images show different phases at different times of the relaxation process of the disk following the perturbation induced by the intense flaring activity. The cutaway views of the star-disk system show the mass density (blue) and the magnetic field lines (green) (run F6f1.00a).
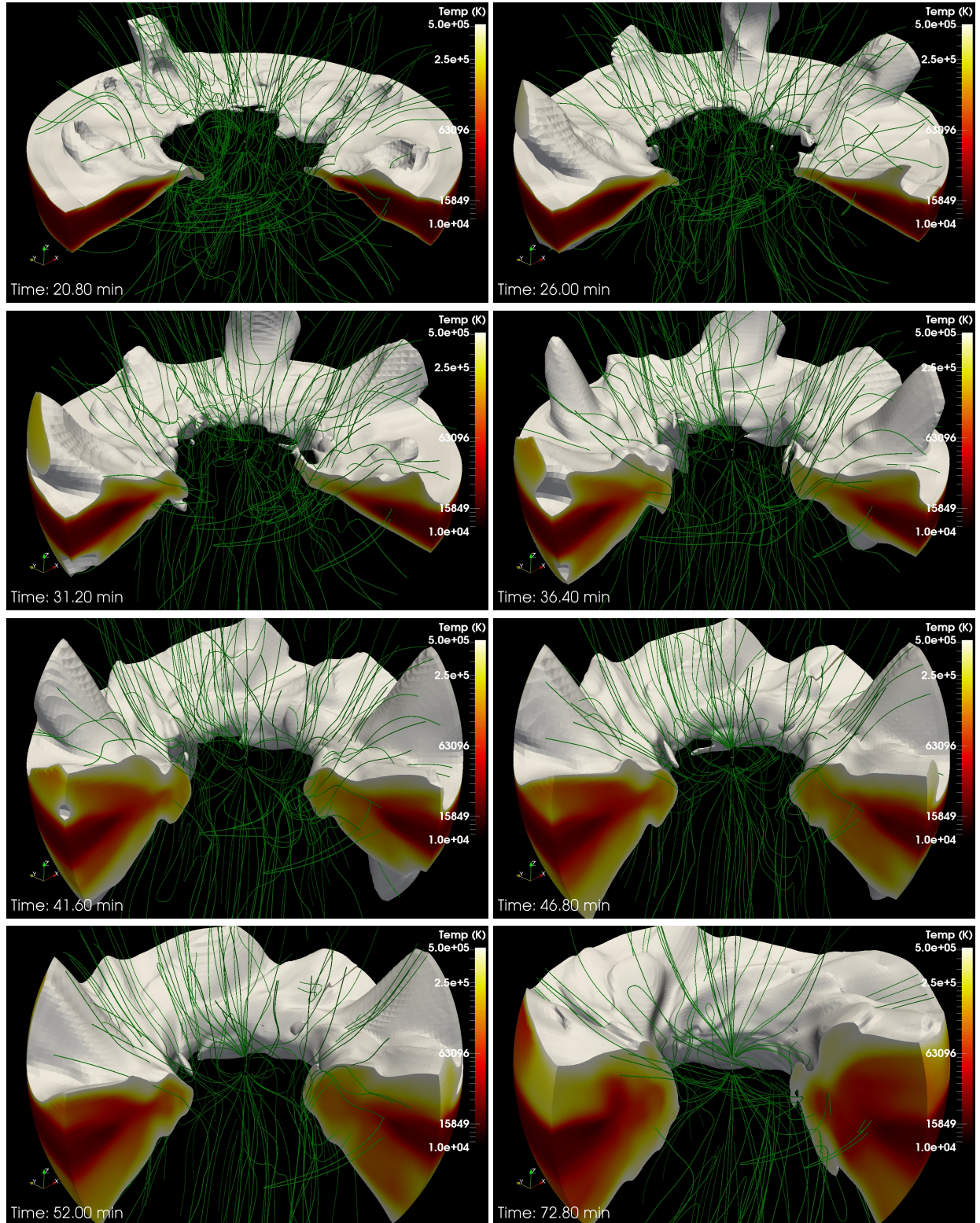
Figure 3.13: The above images show different phases at different times of the relaxation process of the disk following the perturbation induced by the intense flaring activity. The cutaway views of the star-disk system show the temperature of the disk (red-yellow-white) and the magnetic field lines (green) (run F6f1.00a).
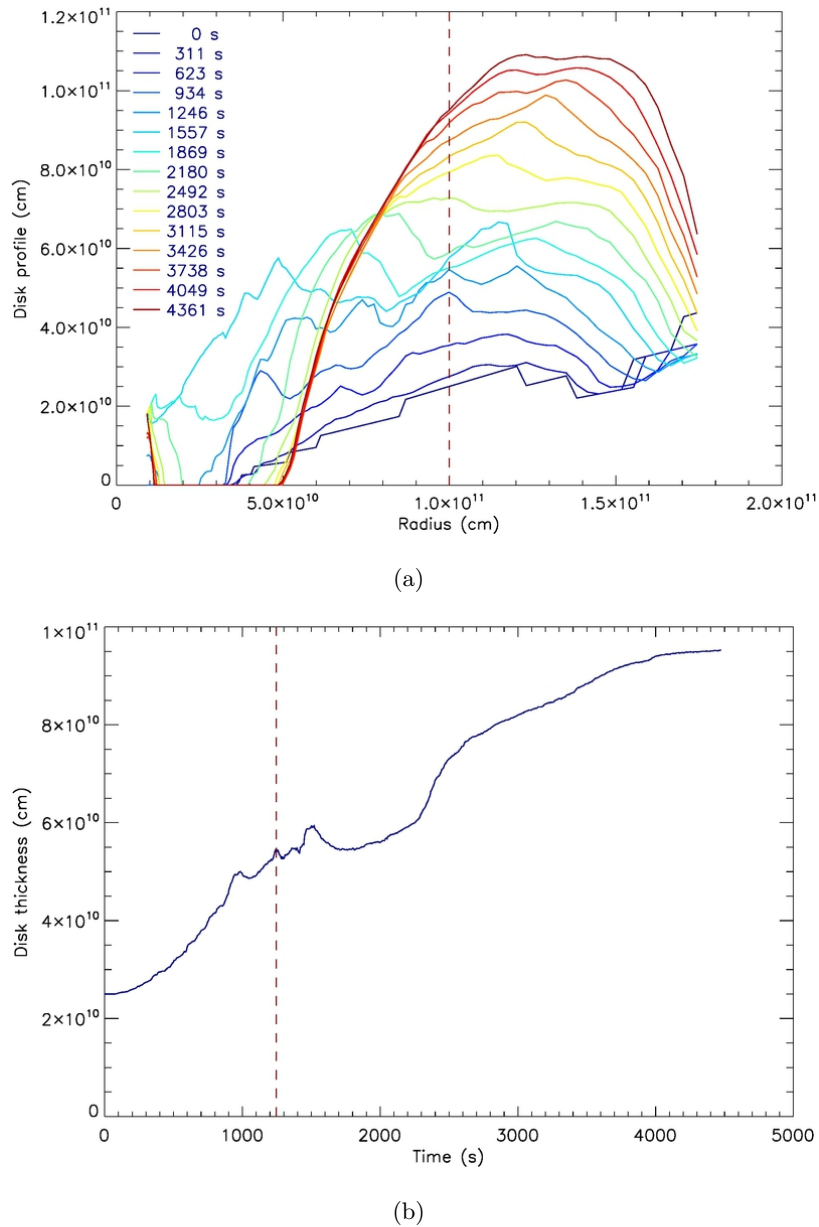
(a)

(b)

Figure 3.14: Evolution of the disk surface in time: (a) profiles of the disk at various times; (b) disk thickness vs. time, this value is obtained averaging over the angle ϕ the height of all the points on the disk surface at half of the radius of the disk (dashed line in the upper plot). The dashed line in the lower graph shows at which time the flaring activity is over ($1246\ s$).

evolution respectively in terms of density values and temperature.

Among these promising preliminary results, the main findings we can deduce from the analysis of these simulations are the following. The disk, albeit swollen and overheated, is not disrupted and the intense flaring activity simulated on its surface, in the specific configuration analysed, was not able to destroy it, in spite of a profound perturbation induced on its structure. Moreover, there is a clear tendency of the disk to relax. Nevertheless,

almost 60 minutes of simulated time is a too short time period to find out if the disk is going to recover to a configuration similar to the pre-flare one and the time needed to do that. In this respect, it is worth noting that the disk, at the system evolution simulated to date, seems to have not completely finished its expansion phase (see Fig. 3.14).

Chapter 4

Summary, conclusions and perspectives

We investigated the effect of an intense flaring activity occurring on the surface of the accretion disk of various *IPCV* prototypes. The several prototypes taken into account consider different values of density and magnetic field. We focused on different aspects: the conditions able to jeopardize the stability of the disk; the formation of an extended corona above the disk; the contribution of the related coronal activity to the thermal X-ray emission from these objects.

We have developed a 3D MHD model taking into account all the key physical processes: viscosity of the disk, magnetic field oriented thermal conduction, radiative cooling and gravitational forces. In order to set up the initial conditions of the 3D simulations, we have devised a two-step technique. As a first step, we have run 2.5D simulations in order to obtain a developed configuration of the magnetic field, from this we have reconstructed a 3D initial condition where we then simulated a hail of flares distributed stochastically on the surface of the inner part of the accretion disk. Finally, we synthesized the thermal X-ray emission from each system all along the whole evolution.

In the light of our findings, we can draw the following main conclusions: (a) an intense flaring activity close to the surface of the accretion disk can build up an extended corona linking the star to the disk along the magnetic field lines; (b) the thermal X-ray emission from the corona is mainly emitted from a thin layer immediately above the surface of the disk; (c) the thermal X-ray luminosity due to the flaring activity may significantly contribute to the emission observed from these objects; (d) this coronal activity is able to influence the disk configuration and its stability, effectively deforming the magnetic field lines, with effects strongly dependent on density and magnetic field intensity. Secondly, we can include among the conclusions the following: (e) the radiative and conductive cooling has a crucial role in the modulation of luminosity due to the chain of flares, and

it has different impact on the lightcurves depending on the X-ray band considered and on the temperature of the emitting plasma, contributing efficaciously to the phenomenon of flickering originating from the inner region of the disk; (f) the accretion rate values found are lower than expected for $IPCV$s and they could be possibly consistent with the model of Ghosh & Lamb (1978) for fast rotators.

It is worth noting that the synthesized thermal X-ray emission exhibits luminosity values ranging between 10^{30} and 10^{32} erg/s. These values, especially those for the high density configurations explored, are in general agreement with previous studies (Patterson et al., 1980; van der Woerd, 1987; Eracleous et al., 1991; Choi et al., 1999; Venter & Meintjes, 2007)

Summarizing, the results presented above suggest that an intense flaring activity occurring on the surface of the accretion disk of $IPCV$ stars may turn out to have an important effects on the structure of the system and its stability, and a key role in the formation of an extended corona, whose effects may contribute remarkably to the thermal X-ray emission observed from these objects.

Our study has brought significant results in the field that allowed to understand how the disk can be perturbed by an intense flaring activity and, on the other hand, how an extended accretion disk corona can develop, contributing to the thermal X-ray emission. Our study also opens new windows of opportunity with respect to further investigations and future perspectives. On one hand, we have developed a working computational model and set up several techniques and data processing tool from scratch. Actually, we have defined a proper framework for additional studies. On the other hand, our study has only started exploring the dynamics of the disk after a strong perturbation as, for example, that produced by an intense flaring activity. In the following we analyse the elements having room for in-depth analysis and deserving further consideration.

The first possible future line of research could be the reproduction of real observed objects through a fine tuning of the various characteristic parameters and quantities of the object we want to reproduce, such as mass, density of the disk, magnetic field. Also, for the synthesis of observational feature, we could take into account also non-thermal emission and specific angles of the line of sight with the equatorial plane.

As a second line of research, we would like to continue to carry on the exploratory relaxation studies whose preliminary results are exposed in Section 3.4, in order to understand under which condition the perturbed accretion disk can recover to a relaxed state similar to the pre-disturbance one.

A third line of research could be related to the accretion. In fact, we have chosen a configuration of the system with a corotation radius coincident with the magnetospheric radius and it would indeed indicate a system in a weak propeller regime, for which low

accretion rate and weak outflows are actually expected. To this end, it would be worth being investigated the effects of a different choice of corotation radius. Indeed, a corotation radius larger than the magnetosheric radius may have major implication on the accretion rate, resulting in possibly more conspicuous accretion phenomena (Lovelace et al., 1999; Romanova et al., 2004).

As a final thought to the possible future perspective of the presented research, one may want to further extend the model to more extreme accreting systems. An interesting field that could be investigated through our model is the one related to the novae explosions, in order to study the dynamics of the blast, its interaction with the magnetic field and the accretion disk, and the related non-thermal emission. To this end, some exploratory simulations are currently running.

Appendix A

Viscous tensor

The general form of the viscosity tensor may be written as follows:

$$\vec{\tau} = \eta_b \left(\nabla \cdot \vec{u} \right) \vec{I} + \eta_s \left[\left(\nabla \vec{u} \right) + \left(\nabla \vec{u} \right)^T - \frac{2}{3} \left(\nabla \cdot \vec{u} \right) \vec{I} \right], \tag{A.1}$$

this appendix gives a brief description of the main elements playing a role in viscosity and provides a magnitude analysis of the various terms in the equation (A.1).

A.1 Bulk viscosity

The first term in in the right-hand side of the equation (A.1) is related to the *bulk viscosity*. It takes into account that a compressible fluid, when uniformly compressed/expanded, shows a sort of internal friction opposing to the compression/expansion. This term can become important only in case of quick compressions/expansions as in sound propagation or in shock waves. The force density related to bulk viscosity can be written as follows:

$$F_b \sim -2\rho c_s \lambda_d \frac{\partial^2 v_x}{\partial x^2} \tag{A.2}$$

where λ_d is the thermal mean free path and we used the fact that the ions of a plasma have thermal velocities of the order of the sound speed c_s (Frank et al., 2002).

A.2 Shear viscosity

The second term in the right-hand side of the equation (A.1) takes into account the action of the *shear viscosity*. It expresses the opposition to motion exhibited by parallel neighbour layers moving with different velocities v_Φ, e.g. the material in a differentially rotating
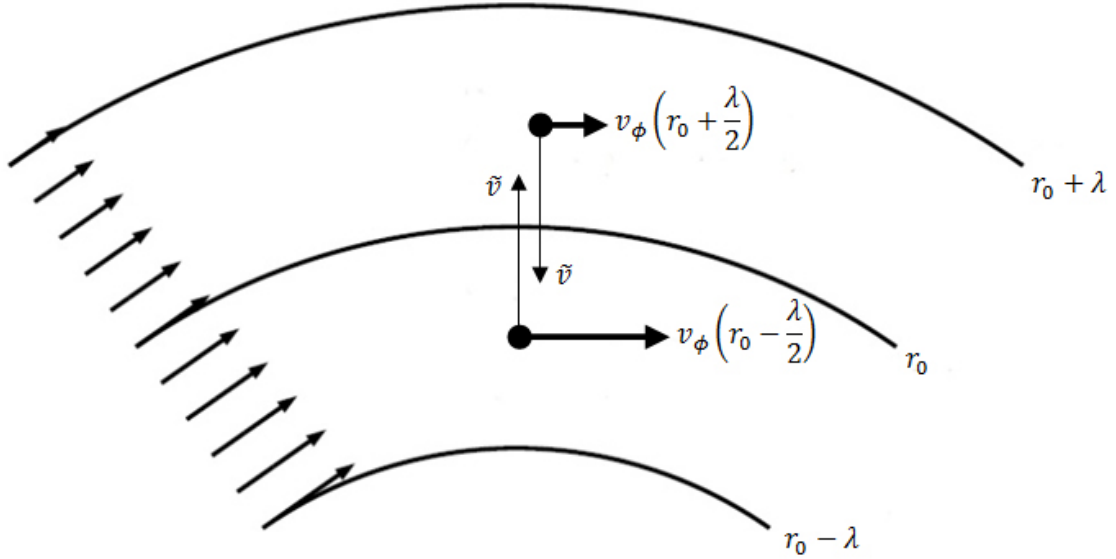
Figure A.1: Schematic representation of the motion of adjacent layers in a differentially rotating environment (e.g. a keplerian disk).

accretion disk at neighbouring radii moving with different angular velocity (see Fig. A.1). The factor η_s is called *dynamic viscosity* and is defined as follows (see also equation (2.7)):

$$\eta_s = \nu_s \rho \tag{A.3}$$

where ρ is the density and ν_s is called *kinematic viscosity*. Shear viscosity gives a viscous torque exerted by a force density in the Φ-direction which is dimensionally identical to the bulk viscous force density of equation (A.2) (Frank et al., 2002):

$$F_s \sim \rho \tilde{v} \lambda \frac{\partial^2 v_\Phi}{\partial r^2} \tag{A.4}$$

where $\tilde{v}$ is the is the speed in the radial direction responsible for the transport of momentum, whilst λ is the radial excursion considered and v_Φ the velocity orthogonal to the radial direction (see Fig. A.1).

A.3   The α-prescription

In order to get a measure of the importance of viscosity, we can define the *Reynolds number* as the ratio between the magnitude of the inertial term $\vec{\nabla} \cdot (\rho \vec{u} \vec{u})$ of the momentum conservation equation (2.2) and the viscous force density:

$$Re = \frac{inertia}{viscosity} \sim \frac{\left(\frac{\rho v^2}{R}\right)}{\left(\rho \lambda u \frac{v}{R^2}\right)}. \tag{A.5}$$

If $Re \ll 1$ viscous forces dominate the flow; otherwise, if $Re \gg 1$, the viscosity associated with the given λ and u is dynamically unimportant. In particular, the second case occurs for the standard 'molecular' bulk viscosity, for which $\lambda \sim \lambda_d$ and $\tilde{v} \sim c_s$. As a matter of fact, in typical regions of an accretion disk the Reynolds number taking into account the molecular viscosity is such that $Re_{mol} > 10^{14}$. However, in general, this number hardly deviates below this estimate (Frank et al., 2002). Thus, molecular viscosity is too weak to be accountable for viscous dissipation and angular momentum transport observed in accretion disks.

Laboratory experiments show that there is a critical Reynolds number (usually Re_{crit} is of the order $10 - 10^3$) at which turbulence starts and the fluid velocity v suddenly begins to exhibit large and chaotic changes on an random timescale and lengthscale. If we suppose that accretion disks are turbulent environment, the plasma flow can be defined by the characteristic size λ_{turb} and the characteristic velocity v_{turb} of the largest eddies (Landau & Lifshitz, 1959; Frisch, 1995). Since the eddies cannot be larger than the disk thickness H, we can suppose $\lambda_{turb} \cong H$. Analogously, the speed of the eddies can be supposed a fraction of the sound speed $v_{turb} = \alpha c_s$ with $\alpha < 1$. Thus, the turbulent cinematic viscosity can be defined as follows:

$$\nu_{turb} = \lambda_{turb} v_{turb} = \alpha c_s H = \alpha \frac{c_s^2}{\Omega} \tag{A.6}$$

where $c_s = \sqrt{\gamma p/\rho}$ is the isothermal sound speed and Ω is the angular velocity of the plasma. The parameter α is a phenomenological dimensionless factor known as the α-*prescription* defined in the Shakura & Sunyaev model taking into account the effect of anomalous viscosity (Shakura & Sunyaev, 1973).

Turbulence is to date a not completely understood phenomenon and the α-*prescription* can be considered only an useful parametrization in order to make theory match with observation. Nevertheless, to date the most promising mechanism in order to explain anomalous viscosity is the Magneto-Rotational Instability (MRI).

Appendix B

Flare energetics

A flare is a sudden, rapid, and intense variation in brightness. The radiation is emitted in a broad band ranging across almost the entire electromagnetic spectrum, from radio waves, through optical, to X-rays possibly up to gamma rays.

The energy released in a solar flare varies from 10^{29} erg to $6 \cdot 10^{32}$ erg or more in the largest events. This energy, that powers flares, comes from the sudden (timescales of minutes to tens of minutes) release of magnetic energy stored in the corona (Priest, 2014).

Basically, the reason of this energy release is that the magnetic field tends to relax to the minimum energy condition. As a matter of fact, the corona is a highly conducting environment in equilibrium where current actually exists. In such a condition the magnetic field is normally in a state called *force-free* for which the Lorentz force vanishes everywhere, being the current parallel to the magnetic field itself. Nevertheless, this configuration of the magnetic field is not the minimum-energy one. The minimum-energy condition is satisfied when the magnetic field is called *potential* or *current-free*. This configuration play a very important role, since a *force-free* magnetic field contains more energy than the corresponding *current-free*, the excess of energy is released through a flare (Sturrock, 1994).

B.1 *Force-free* and *Current-free* fields

Consider the momentum conservation equation, written in the following formalism (Priest, 2014)

$$\rho \frac{d\vec{v}}{dt} = -\vec{\nabla} p_t + \frac{(\vec{j} \times \vec{B})}{c} + \rho \vec{g}. \tag{B.1}$$

The inertial term on the left-hand side of the equation (B.1) may be neglected when the the bulk velocity of plasma is much smaller than, respectively, sound speed (c_s), Alfvén speed (v_A) and gravitational free-fall velocity (v_{ff}):

$$v \ll \begin{cases} c_s = \sqrt{\frac{\gamma p_0}{\rho_0}} \\ \\ v_A = \frac{B_0}{\sqrt{4\pi\rho_0}} \\ \\ v_{ff} = \sqrt{2gl_0}. \end{cases} \tag{B.2}$$

Moreover, depending on circumstances, the terms in equation (B.1) are not equally important. As a matter of fact, if the typical size of the system is much smaller than the *pressure-scale-height*[1], the gravitational term is negligible compared to pressure gradient. Analogously, if the β of the plasma is $\ll 1$, the magnetic field dominates the system, and pressure gradient is negligible compared to the Lorentz force. Therefore, under these conditions, we can write equation (B.1) as follows:

$$0 = \vec{j} \times \vec{B}. \tag{B.3}$$

Equation (B.3) entails that the current flows along field lines, namely $\vec{j} = k\vec{B}$ and magnetic fields satisfying this condition are called *force-free*.

A special case of *force-free* magnetic field is called *current-free*. This particular configuration is realized when equation (B.3) is fulfilled by a zero current:

$$\begin{aligned} \vec{j} = 0 \;\; &\Rightarrow \;\; \frac{c}{4\pi}\vec{\nabla} \times \vec{B} = 0 \;\; \Rightarrow \;\; \frac{c}{4\pi}[\vec{\nabla} \times (\vec{\nabla} \times \vec{B})] = 0 \\ &\Rightarrow \;\; \frac{c}{4\pi}[\vec{\nabla}(\vec{\nabla} \cdot \vec{B}) - \nabla^2 B] = 0 \;\; \Rightarrow \;\; \nabla^2 B = 0, \end{aligned} \tag{B.4}$$

i.e. $\vec{B}$ yields the vector Laplace equation and it is called *potential*, being written

$$\vec{B} = \vec{\nabla}\Psi \;\; \Rightarrow \;\; \vec{\nabla} \cdot \vec{B} = \vec{\nabla} \cdot \vec{\nabla}\Psi \;\; \Rightarrow \;\; \nabla^2\Psi = 0. \tag{B.5}$$

where Ψ is the scalar magnetic potential satisfying the scalar Laplace equation.

B.2   Magnetic minimum-energy theorem

Consider a surface S and suppose that $\vec{B}_0$ is a potential magnetic field; $\vec{B}$ a generic magnetic field having the same normal component to the surface of the potential one ($B_n = B_{0n}$);

---

[1]Distance over which the pressure varies by a factor of e.

and, finally, $\vec{B}_1$ another generic field with zero normal component, such that $\vec{B} = \vec{B}_0 + \vec{B}_1$. In Fig. B.1 a schematic representation of the magnetic field components considered is shown.

Then, using an useful vector identity along with the fact that $\vec{\nabla} \cdot \vec{B}_1 = 0$, and the divergence theorem, the energy stored in the magnetic field $\vec{B}$ can be written as follows:

$$
\begin{aligned}
W = \int_V \frac{B^2}{8\pi} dV &= \int_V \frac{B_0^2}{8\pi} dV + \int_V \frac{B_1^2}{8\pi} dV + \int_V \frac{\vec{B}_0 \cdot \vec{B}_1}{4\pi} dV \\
&= E_0 + E_1 + \int_V \frac{\vec{\nabla}\Psi \cdot \vec{B}_1}{4\pi} dV \\
&= E_0 + E_1 + \frac{1}{4\pi} \int_V \vec{\nabla} \cdot (\Psi \vec{B}_1) - \Psi \vec{\nabla} \cdot \vec{B}_1 dV \\
&= E_0 + E_1 + \frac{1}{4\pi} \oint_S \Psi \vec{B}_1 \cdot \hat{n} dS = E_0 + E_1 > E_0.
\end{aligned}
\tag{B.6}
$$

Equation (B.6) yields that W in general exceeds the energy of the potential field B_0, as required, since $B_1^2 > 0$.

This result means that a non-zero-current magnetic field (e.g. *force-free*), contains more energy than a *current-free* (potential) magnetic field. It is just the presence of non-vanishing currents that increase the total magnetic energy. Hence, the potential magnetic field contains the minimum amount of energy (Priest, 2014).

This fundamental theorem typically finds a clear application in flare dynamics. As a matter of fact, if we consider a potential magnetic field as a starting configuration, the moving plasma will generate current capable to generating new non-current-free magnetic field components. When a flare is triggered the excess energy is released in order to get back to a minimum energy potential configuration of the field.
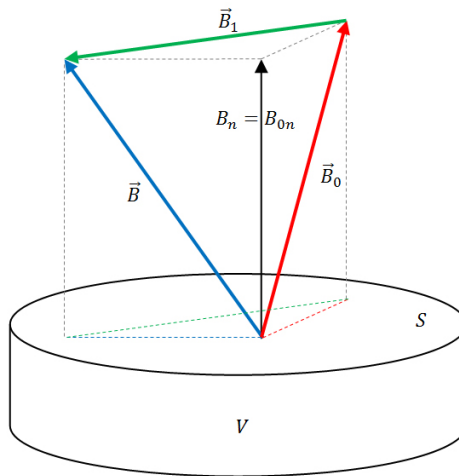

Figure B.1: Schematic representation of magnetic fields, where $\vec{B}_0$ is the potential one.

B.3   Magnetic energy release

So far we can define a flare as an event triggered by an instability of the underlying magnetic field configuration that relaxes into a more stable state by changing and reconnecting the magnetic topology. This change in magnetic topology provides a release of nonpotential magnetic energy through currents in the form

$$\vec{\nabla} \times \vec{B} = \frac{4\pi}{c} \vec{j}.$$

(B.7)

These currents produce plasma heating and particle acceleration and their presence must be taken into account in the MHD equations, in particular in energy equation and in induction equation. The energy conservation equation can be written as follows:

$$\frac{\partial}{\partial t}(\rho E + \frac{\rho u^2}{2}) + \vec{\nabla} \cdot [(\rho E + \frac{\rho u^2}{2})\vec{u}] = -\vec{\nabla} \cdot \vec{u}P_t + \rho\vec{u} \cdot \vec{g} - \vec{\nabla} \cdot \vec{F_c}$$
$$- n_e n_H \Lambda(T) + (\vec{E} \cdot \vec{j} - \frac{j^2}{\sigma})$$

(B.8)

where the terms in the right hand side of the equation are respectively the work done by pressure, the gravitational energy, the heat flow, the radiative losses and, finally, the electrical energy, for which σ is the conductivity (Priest, 2014). As for the induction equation, we can write it in the following manner:

$$\frac{\partial \vec{B}}{\partial t} = -c\vec{\nabla} \times \vec{E} = -c\vec{\nabla} \times \left(\frac{\vec{j}}{\sigma} - \frac{\vec{u} \times \vec{B}}{c} \right)$$
$$= \frac{c^2}{4\pi\sigma}\vec{\nabla} \times \left(\vec{\nabla} \times \vec{B} \right) + \vec{\nabla} \times \left(\vec{u} \times \vec{B} \right)$$
$$= \eta\nabla^2\vec{B} + \vec{\nabla} \times (\vec{u} \times \vec{B})$$

(B.9)

where $\eta = c^2/(4\pi\sigma)$ is the magnetic diffusivity. The current can be dissipated by Joule heating of the plasma and η, through σ, determines the Joule heating time scale τ_J. In fact, the electrical conductivity may be written as:

$$\sigma = \frac{n_e e^2 \tau_{ce}}{m_e} \propto T_e^{\frac{3}{2}}$$

(B.10)

where τ_{ce} is the electron collision time and T_e the electron temperature. It is possible to define a Joule heating time scale as follows:

$$\tau_J = \frac{n_e k_B T_e}{\vec{j} \cdot \vec{E}}, \tag{B.11}$$

being the total energy dissipated by a current density j given by $\vec{j} \cdot \vec{E}$ (Aschwanden, 2005).

A significant plasma heating can only occur when the Joule heating time τ_J is shorter than the radiative or conductive cooling time. From this constraint, Holman (1985) finds that the resistivity must be much greater than the classical resistivity in (hot) quiet solar corona conditions where $n_e \approx 10^9 \ cm^{-3}$ and $T_e = 10^7$. For flares, a plasma density of $n_e > 10^{11} \ cm^{-3}$ is required, otherwise, in the case of lower densities, the presence of an anomalous resistivity must be taken into account.

The classical resistivity stems from frictional forces in Coulomb collisions between electrons and ions of the same temperature. On the other hand, anomalous resistivity occurs in plasmas in a turbulent state (Coppi & Friedland, 1971). In these conditions, the electrons carrying the current also interact with the electric field of different types of waves (e.g. electrostatic ion-cyclotron waves, ion-acoustic waves), that are able to change the resistivity and other transport coefficients (Aschwanden, 2005).

In order to define this anomalous resistivity, the key question is: when a field is stressed to a force-free state by the motion of the plasma at the footpoints, for how long does energy build up before an energy release with the subsequent heating event occurs? Actually, when the current density exceeds a critical value $\left(j_{cr} = 75 \ A \ cm^{-2}\right)$, anomalous resistivity $\left(\eta = 10^{14} \ cm^2 \ s^{-1}\right)$ switches on. Then, after an initial reconnection phase in a single current sheet, the fast reconnection is triggered, and the current sheet splits up into multiple reconnection sites to give almost full relaxation and heating throughout the flux rope (Hood et al., 2009; Priest, 2014).

Appendix C

Elements of computational physics

This appendix provides additional details about some of the numerical techniques used in the present work. In particular, some methods used by the PLUTO code in order to solve the MHD equations are described.

C.1 Dimensionless MHD equation

Writing the MHD equations in a non dimensional form may result extremely useful in order to obtain numerical solutions. Through the MHD module, the PLUTO code solves a set of four time-dependent MHD equations defined in a 3D spherical coordinate system $(r,\ \theta,\ \phi)$. The classical MHD equations (2.1 - 2.4), extended to include gravitational force, viscosity, thermal conduction, radiative cooling and plasma heating, are solved in a conservative and non dimensional form as follows:

$$\frac{\partial \rho}{\partial t} + \nabla \cdot (\rho \vec{u}) = 0 \qquad\qquad \textit{Mass conservation eq.}$$
$$(\text{C.1})$$

$$\frac{\partial \rho \vec{u}}{\partial t} + \nabla \cdot (\rho \vec{u} \vec{u}) = \nabla \cdot \left(\vec{B}\vec{B} - \vec{I}P_t + \vec{\tau} \right) + \rho \vec{g} \qquad\qquad \textit{Momentum conservation eq.}$$
$$(\text{C.2})$$

$$\frac{\partial \rho E}{\partial t} + \nabla \cdot (\rho E \vec{u}) = \nabla \cdot \left[-\vec{u}P_t + \vec{B} \left(\vec{u} \cdot \vec{B} \right) + \vec{u} \cdot \vec{\tau} \right]$$
$$+ \rho \vec{u} \cdot \vec{g} - \nabla \cdot \vec{F_c} - n_e n_H \Lambda\left(T\right) + Q\left(r, \theta, \phi, t\right) \qquad \textit{Energy conservation eq.}$$
$$(\text{C.3})$$

$$\frac{\partial \vec{B}}{\partial t} + \nabla \cdot \left(\vec{u}\vec{B} - \vec{B}\vec{u} \right) = 0 \qquad\qquad \textit{Induction eq.}$$
$$(\text{C.4})$$

where the total pressure (P_t) is the sum of thermal and magnetic pressure, and the total energy per unit of mass (E) is the sum of internal or thermal (ϵ), kinetic (E_k) and magnetic energy (E_{mag}):

$$P_t = P + \frac{\vec{B} \cdot \vec{B}}{2}; \qquad E = \epsilon + E_k + E_{mag} = \epsilon + \frac{\vec{u} \cdot \vec{u}}{2} + \frac{\vec{B} \cdot \vec{B}}{2\rho}. \qquad \text{(C.5)}$$

The mass density is defined as $\rho = \mu m_H n_H$, where m_H is the mass of hydrogen atom, n_H is the number of hydrogen atoms per unit of volume, and μ is the mean atomic mass. The bulk velocity of the plasma is defined as $\vec{u}$.

C.2   Godunov's scheme

PLUTO code is designed to be a Godunov-type code, that means that the numerical solution of a generic hyperbolic conservation law in the form

$$\frac{\partial u}{\partial t} = -\vec{\nabla} \cdot \vec{\Phi}_u + S_u, \qquad \text{(C.6)}$$

where u represents a set of conservative quantities, Φ_u is the flux tensor and S_u defines the source terms, can be approximated by the following formulation of a finite volume method:

$$u_i^{n+1} - u_i^n = -\frac{\Delta t}{\Delta x} \left(\Phi_{i+\frac{1}{2}}^n - \Phi_{i-\frac{1}{2}}^n \right) + S_u \qquad \text{(C.7)}$$

where the subscript i define the i-th spatial element of a finite elements grid, whilst the superscript n refers to the n-th time step. Godunov's method solves the Riemann problem at each cell boundary exactly. For non-linear systems of conservation laws this is often all but a easy task, because an iterative procedure is often required which, since this must be done at every cell boundary at every time step, it represents the most computationally expensive part of the method.

However, to simplify the process and reduce the computational load, variants of the method have been devised by utilizing approximate Riemann solvers which do not employ iteration. For these reasons, PLUTO were configured to compute inter-cell fluxes with the Harten-Lax-Van Leer (HLL) approximate Riemann solver.

C.3 Time stepping and the Runge-Kutta method

The $n-$th time step $\Delta t^{(n)}$ represents the time increment between two consecutive steps $\left(t^{(n+1)} - t^{(n)}\right)$ and is computed using the information available from the previous $(n-1)-$th time-step. $\Delta t^{(n)}$ can be controlled by the Courant-Friedrichs-Lewy (CFL) number C_a and must obey the following condition:

$$\Delta t^{(n)} \max_{ijk} \left[\frac{1}{N_{dim}} \sum_d \left(\frac{\lambda_d}{\Delta l_d} + \frac{2\tau_d}{\Delta l_d^2} \right) \right] = C_a \leq \frac{1}{N_{dim}} \tag{C.8}$$

where for a given direction d, Δl_d is the computational cell physical length, λ_d is the largest signal speed, τ_d accounts for diffusion processes. Once the $n-$th time step $\Delta t^{(n)}$ is computed, the time solution of the problem is obtained through a second order Runge-Kutta (RK2) scheme. This method advances the solution to the next time level using an intermediate step u^*, as follows:

$$
\begin{aligned}
&u^{(n)} \\
&\downarrow \\
&u^{(*)} = u^{(n)} + \Delta t^{(n)} \mathcal{L}^{(n)} \\
&\downarrow \\
&u^{(n+1)} = \frac{1}{2} \left(u^{(n)} + u^{(*)} + \Delta t^{(n)} \mathcal{L}^{(*)} \right)
\end{aligned}
\tag{C.9}
$$

where $u^{(i)}$ is the solution at the time $t^{(i)}$ and $\mathcal{L}$ denotes the discretized spatial operator on the right hand side of equation (C.6).

C.4 Power law distribution generation

In this section we describe the general technique used to get a power-law distribution from a uniform distribution, which is what most random number generators provide. First of all let's consider a power law function, whose aspect is depicted in Fig. C.1, defined as follows:

$$P(x) = cx^n. \tag{C.10}$$

Then, we normalize to unity the integral of this function between x_0 and x_1:

$$\int_{x_0}^{x_1} P(x)dx = \int_{x_0}^{x_1} cx^n dx = c \left[\frac{x^{n+1}}{n+1} \right]_{x_0}^{x_1} = 1, \tag{C.11}$$
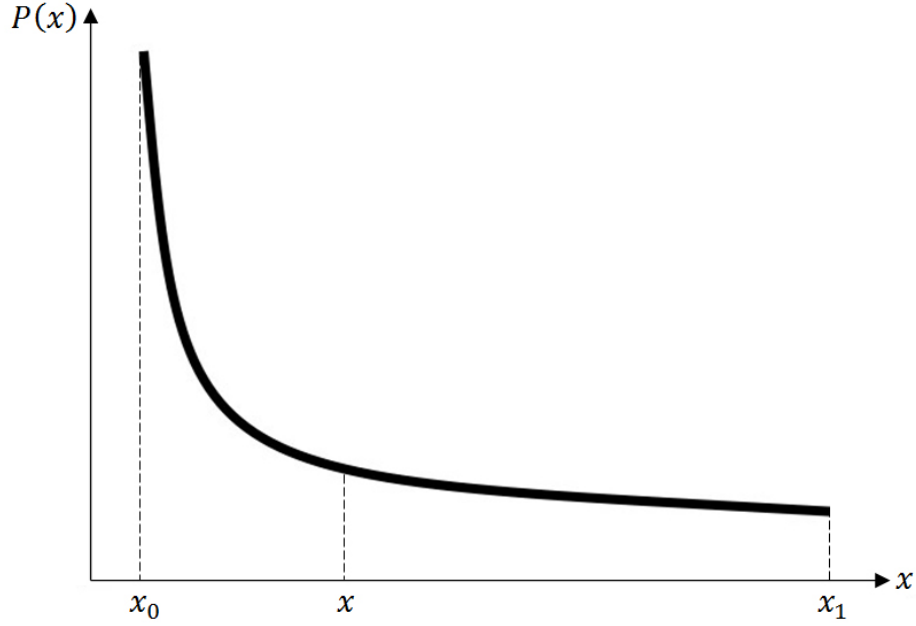
Figure C.1: Schematic representation of the power law function.

from equation (C.11) we obtain the normalization factor c:

$$c = \frac{n+1}{x_1^{n+1} - x_0^{n+1}}. \tag{C.12}$$

Analogously to equation (C.11), we can calculate the integral between x_0 and a generic $x < x_1$. The value of this integral will be equal to a value y between 0 and 1, as follows:

$$\int_{x_0}^{x} P(t)dt = \int_{x_0}^{x} ct^n dt = c \left[\frac{t^{n+1}}{n+1} \right]_{x_0}^{x} = \frac{c}{n+1} \left(x^{n+1} - x_0^{n+1} \right) = y\epsilon\,[0,1]. \tag{C.13}$$

Using c we obtain x as a function of y:

$$x = \left[\frac{n+1}{c} y + x_0^{n+1} \right]^{\frac{1}{n+1}} = \left[\left(x_1^{n+1} - x_0^{n+1} \right) y + x_0^{n+1} \right]^{\frac{1}{n+1}}. \tag{C.14}$$

Equation (C.14) yields a variable x following a power law distribution from a uniformly distributed y between $[0, 1]$.

In particular, in the study here presented, the variable x represents a fraction, ranging between 0.01 and 1, of the maximum intensity of the flares, whereas the power $n = \alpha = -2.1$. Hence, this technique allows to generate flares having a recurrence progressively decreasing with their intensity, so there will be more flare with low or medium than high intensity.

Acknowledgements

References

Alexiades, V., Amiez, G., & Gremaud, P.-A. (1996). Super-time-stepping acceleration of explicit schemes for parabolic problems. *Communications in Numerical Methods in Engineering*, *12*(1), 31–42. Retrieved from http://dx.doi.org/10.1002/(SICI)1099-0887(199601)12:1<31::AID-CNM950>3.0.CO;2-5 doi: 10.1002/(SICI)1099-0887(199601)12:1⟨31::AID-CNM950⟩3.0.CO;2-5

Anders, E., & Grevesse, N. (1989, January). Abundances of the elements - Meteoritic and solar. *Geochim. Cosmochim. Acta*, *53*, 197-214. doi: 10.1016/0016-7037(89)90286-X

Armitage, P. J., & Clarke, C. J. (1996, May). Magnetic braking of T Tauri stars. *MNRAS*, *280*, 458-468. doi: 10.1093/mnras/280.2.458

Aschwanden, M. J. (2005). *Physics of the Solar Corona. An Introduction with Problems and Solutions (2nd edition)*.

Balbus, S. A. (2003). Enhanced Angular Momentum Transport in Accretion Disks. *ARA&A*, *41*, 555-597. doi: 10.1146/annurev.astro.41.081401.155207

Balsara, D. S., & Spicer, D. S. (1999, March). A Staggered Mesh Algorithm Using High Order Godunov Fluxes to Ensure Solenoidal Magnetic Fields in Magnetohydrodynamic Simulations. *Journal of Computational Physics*, *149*, 270-292. doi: 10.1006/jcph.1998.6153

Balucinska-Church, M., & McCammon, D. (1992, December). Photoelectric absorption cross sections with variable abundances. *ApJ*, *400*, 699. doi: 10.1086/172032

Bessolaz, N., Zanni, C., Ferreira, J., Keppens, R., & Bouvier, J. (2008, January). Accretion funnels onto weakly magnetized young stars. *A&A*, *478*, 155-162. doi: 10.1051/0004-6361:20078328

Borkowski, K. J., Shull, J. M., & McKee, C. F. (1989, January). Two-temperature radiative shocks with electron thermal conduction. *ApJ*, *336*, 979-998. doi: 10.1086/167069

Brown, J. C., Spicer, D. S., & Melrose, D. B. (1979, March). Production of a collisionless conduction front by rapid coronal heating and its role in solar hard X-ray bursts. *ApJ*, *228*, 592-597. doi: 10.1086/156883

Bruch, A. (2015, July). Time lags of the flickering in cataclysmic variables as a function of wavelength. *A&A*, *579*, A50. doi: 10.1051/0004-6361/201425393

Choi, C.-S., Dotani, T., & Agrawal, P. C. (1999, November). A Study of the X-Ray Emission of the Magnetic Cataclysmic Variable AE Aquarii. *ApJ*, *525*, 399-406. doi: 10.1086/307873

Church, M. J., & Bałucińska-Church, M. (2004, March). Measurements of accretion disc corona size in LMXB: consequences for Comptonization and LMXB models. *MNRAS*, *348*, 955-963. doi: 10.1111/j.1365-2966.2004.07162.x

Coppi, B., & Friedland, A. B. (1971, October). Processes of Magnetic-Energy Conversion and Solar Flares. *ApJ*, *169*, 379. doi: 10.1086/151150

Cowie, L. L., & McKee, C. F. (1977, January). The evaporation of spherical clouds in a hot gas. I - Classical and saturated mass loss rates. *ApJ*, *211*, 135-146. doi: 10.1086/154911

Dhillon, V. S. (1996). Cataclysmic Variables and Related Objects. In A. Evans & J. H. Wood (Eds.), *Cataclysmic Variables and related objects: Proceedings of the 158th Colloquium of the International Astronomical Union, held at Keele, United Kingdom, june 26–30, 1995* (Vol. 208, p. 3). doi: 10.1007/978-94-009-0325-8_1

Eracleous, M., Halpern, J., & Patterson, J. (1991, November). X-ray spectra of cataclysmic variables from the Einstein Observatory. *ApJ*, *382*, 290-300. doi: 10.1086/170716

Fadeyev, Y. A., Le Coroller, H., & Gillet, D. (2002, September). The structure of radiative shock waves. IV. Effects of electron thermal conduction. *A&A*, *392*, 735-740. doi: 10.1051/0004-6361:20020995

Favata, F., Flaccomio, E., Reale, F., Micela, G., Sciortino, S., Shang, H., . . . Feigelson, E. D. (2005, October). Bright X-Ray Flares in Orion Young Stars from COUP: Evidence for Star-Disk Magnetic Fields? *ApJS*, *160*, 469-502. doi: 10.1086/432542

Ferland, G. J., Korista, K. T., Verner, D. A., Ferguson, J. W., Kingdon, J. B., & Verner, E. M. (1998, July). CLOUDY 90: Numerical Simulation of Plasmas and Their Spectra. *PASP*, *110*, 761-778. doi: 10.1086/316190

Ferland, G. J., Porter, R. L., van Hoof, P. A. M., Williams, R. J. R., Abel, N. P., Lykins, M. L., . . . Stancil, P. C. (2013, April). The 2013 Release of Cloudy. *RMxAA*, *49*, 137-163.

Frank, J., King, A., & Raine, D. J. (2002). *Accretion Power in Astrophysics: Third Edition.*

Frisch, U. (1995). *Turbulence. The legacy of A. N. Kolmogorov.*

Galeev, A. A., Rosner, R., & Vaiana, G. S. (1979, April). Structured coronae of accretion disks. *ApJ*, *229*, 318-326. doi: 10.1086/156957

Ghosh, P., & Lamb, F. K. (1978, July). Disk accretion by magnetic neutron stars. *ApJ*, *223*, L83-L87. doi: 10.1086/182734

Giovannelli, F., Sabau-Graziati, L., & VOID, V. (2012). The golden age of cataclysmic variables and related objects. A review. *Mem. Soc. Astron. Italiana*, *83*, 446.

Giuliani, J. L., Jr. (1984, February). On the dynamics in evaporating cloud envelopes. *ApJ*, *277*, 605-614. doi: 10.1086/161731

Hellier, C. (1993, September). The accretion stream in intermediate polar binaries. *PASP*, *105*, 966-968. doi: 10.1086/133264

Hellier, C. (1997, October). The size of the accretion region in intermediate polars: eclipses of XY ARIETIS observed with RXTE. *MNRAS*, *291*, 71-80. doi: 10.1093/mnras/291.1.71

Hellier, C. (2001). *Cataclysmic variable stars.* Springer.

Hellier, C. (2007, May). Disc magnetosphere interactions in cataclysmic variable stars. In J. Bouvier & I. Appenzeller (Eds.), *Star-disk interaction in young stars* (Vol. 243, p. 325-336). doi: 10.1017/S1743921307009684

Holman, G. D. (1985, June). Acceleration of runaway electrons and Joule heating in solar flares. *ApJ*, *293*, 584-594. doi: 10.1086/163263

Hood, A. W., Browning, P. K., & van der Linden, R. A. M. (2009, November). Coronal heating by magnetic reconnection in loops with zero net current. *A&A*, *506*, 913-925. doi: 10.1051/0004-6361/200912285

Horne, K., & Stiening, R. F. (1985, October). Eclipse maps of the accretion disc in RW Trianguli. *MNRAS*, *216*, 933-948. doi: 10.1093/mnras/216.4.933

Hujeirat, A. (2005, May). A problem-orientable numerical algorithm for modeling multi-dimensional radiative MHD flows in astrophysics the hierarchical solution scenario. *Computer Physics Communications*, *168*, 1-24. doi: 10.1016/j.cpc.2005.01.013

Hujeirat, A., & Camenzind, M. (2000, October). Truncated disks - advective tori solutions around BHs. I. The effects of conduction and enhanced Coulomb coupling. *A&A*, *362*, L41-L44.

Ishida, M., Matsuzaki, K., Fujimoto, R., Mukai, K., & Osborne, J. P. (1997, May). Detailed X-ray spectroscopy of AM Herculis with ASCA. *MNRAS*, *287*, 651-662. doi: 10.1093/mnras/287.3.651

Landau, L. D., & Lifshitz, E. M. (1959). *Fluid mechanics*.

Lovelace, R. V. E., Romanova, M. M., & Bisnovatyi-Kogan, G. S. (1999, March). Magnetic Propeller Outflows. *ApJ*, *514*, 368-372. doi: 10.1086/306945

Mignone, A., Bodo, G., Massaglia, S., Matsakos, T., Tesileanu, O., Zanni, C., & Ferrari, A. (2007, May). PLUTO: A Numerical Code for Computational Astrophysics. *ApJS*, *170*, 228-242. doi: 10.1086/513316

Mukai, K., Rana, V., Bernardini, F., & de Martino, D. (2015, July). Unambiguous Detection of Reflection in Magnetic Cataclysmic Variables: Joint NuSTAR-XMM-Newton Observations of Three Intermediate Polars. *ApJ*, *807*, L30. doi: 10.1088/2041-8205/807/2/L30

Norton, A. J. (1993, November). Simulation of the X-Ray Lightcurves of Intermediate Polars. *MNRAS*, *265*, 316. doi: 10.1093/mnras/265.2.316

Norton, A. J., Beardmore, A. P., Allan, A., & Hellier, C. (1999, July). YY Draconis and V709 Cassiopeiae: two intermediate polars with weak magnetic fields. *A&A*, *347*, 203-211.

Orlando, S., Bocchino, F., Reale, F., Peres, G., & Pagano, P. (2008, May). The Importance of Magnetic-Field-Oriented Thermal Conduction in the Interaction of SNR Shocks with Interstellar Clouds. *ApJ*, *678*, 274-286. doi: 10.1086/529420

Orlando, S., Drake, J. J., & Laming, J. M. (2009, January). Three-dimensional modeling of the asymmetric blast wave from the 2006 outburst of RS Ophiuchi: Early X-ray emission. *A&A*, *493*, 1049-1059. doi: 10.1051/0004-6361:200810109

Orlando, S., Peres, G., Reale, F., Bocchino, F., Rosner, R., Plewa, T., & Siegel, A. (2005, December). Crushing of interstellar gas clouds in supernova remnants. I. The role of thermal conduction and radiative losses. *A&A*, *444*, 505-519. doi: 10.1051/0004-6361:20052896

Orlando, S., Reale, F., Peres, G., & Mignone, A. (2011, August). Mass accretion to young stars triggered by flaring activity in circumstellar discs. *MNRAS*, *415*, 3380-3392. doi: 10.1111/j.1365-2966.2011.18954.x

Patterson, J. (1984, April). The evolution of cataclysmic and low-mass X-ray binaries. *ApJS*, *54*, 443-493. doi: 10.1086/190940

Patterson, J. (1994, March). The DQ Herculis stars. *PASP*, *106*, 209-238. doi: 10.1086/133375

Patterson, J., Branch, D., Chincarini, G., & Robinson, E. L. (1980, September). 33 second X-ray pulsations in AE Aquarii. *ApJ*, *240*, L133-L136. doi: 10.1086/183339

Powell, K. G., Roe, P. L., Linde, T. J., Gombosi, T. I., & Zeeuw, D. L. D. (1999). A solution-adaptive upwind scheme for ideal magnetohydrodynamics. *Journal of Computational Physics*, *154*(2), 284 - 309. Retrieved from http://www.sciencedirect.com/science/article/pii/S002199919996299X doi: http://dx.doi.org/10.1006/jcph.1999.6299

Priest, E. (2014). *Magnetohydrodynamics of the Sun.* Cambridge, UK: Cambridge University Press.

Putney, A. (1999). Magnetic white dwarf stars - a review. In S.-E. Solheim & E. G. Meistas (Eds.), *11th european workshop on white dwarfs* (Vol. 169, p. 195).

Ramsay, G., Cropper, M., Hellier, C., & Wu, K. (1998, July). A comparison of white dwarf mass estimators using the intermediate polar XY Ari. *MNRAS*, *297*, 1269-1273. doi: 10.1046/j.1365-8711.1998.01609.x

Reale, F., & Orlando, S. (2008, September). Nonequilibrium of Ionization and the Detection of Hot Plasma in Nanoflare-heated Coronal Loops. *ApJ*, *684*, 715-724. doi: 10.1086/590338

Reale, F., Orlando, S., Guarrasi, M., Mignone, A., Peres, G., Hood, A. W., & Priest, E. R. (2016, October). 3D MHD modeling of twisted coronal loops. *ApJ*, *830*, 21. doi: 10.3847/0004-637X/830/1/21

Romanova, M. M., Ustyugova, G. V., Koldoba, A. V., & Lovelace, R. V. E. (2002, October). Magnetohydrodynamic Simulations of Disk-Magnetized Star Interactions in the Quiescent Regime: Funnel Flows and Angular Momentum Transport. *ApJ*, *578*, 420-438. doi: 10.1086/342464

Romanova, M. M., Ustyugova, G. V., Koldoba, A. V., & Lovelace, R. V. E. (2004, December). The Propeller Regime of Disk Accretion to a Rapidly Rotating Magnetized Star. *ApJ*, *616*, L151-L154. doi: 10.1086/426586

Salz, M., Banerjee, R., Mignone, A., Schneider, P. C., Czesla, S., & Schmitt, J. H. M. M. (2015, April). TPCI: the PLUTO-CLOUDY Interface . A versatile coupled photoionization hydrodynamics code. *A&A*, *576*, A21. doi: 10.1051/0004-6361/201424330

Seward, F. D., & Charles, P. A. (2010). *Exploring the X-ray Universe.*

Shakura, N. I., & Sunyaev, R. A. (1973). Black holes in binary systems. Observational appearance. *A&A*, *24*, 337-355.

Smith, R. K., Brickhouse, N. S., Liedahl, D. A., & Raymond, J. C. (2001, August). Collisional Plasma Models with APEC/APED: Emission-Line Diagnostics of Hydrogen-like and Helium-like Ions. *ApJ*, *556*, L91-L95. doi: 10.1086/322992

Spitzer, L. (1962). *Physics of Fully Ionized Gases.* Interscience Publishers.

Sturrock, P. A. (1994). *Plasma Physics.*

Tamburini, F., de Martino, D., & Bianchini, A. (2009, July). Analysis of the white-light flickering of the intermediate polar V709 Cassiopeiae with wavelets and Hurst analysis. *A&A*, *502*, 1-5. doi: 10.1051/0004-6361/200911656

Tanaka, T. (1994, April). Finite volume TVD scheme on an unstructured grid system for three-dimensional MHD simulation of inhomogeneous systems including strong background potential fields. *Journal of Computational Physics*, *111*(2), 381–389. Retrieved from http://www.sciencedirect.com/science/article/pii/S0021999184710710 doi: http://dx.doi.org/10.1006/jcph.1994.1071

van der Woerd, H. (1987, February). X-ray emission from non-magnetic cataclysmic variables. *Ap&SS*, *130*, 225-233. doi: 10.1007/BF00654999

Venter, L. A., & Meintjes, P. J. (2007, June). A tenuous X-ray corona enveloping AE Aquarii. *MNRAS*, *378*, 681-690. doi: 10.1111/j.1365-2966.2007.11813.x

Warner, B. (1996, September). Torques and Instabilities in Intermediate Polars. *Ap&SS*, *241*, 263-294. doi: 10.1007/BF00645229

Zanni, C., & Ferreira, J. (2009, December). MHD simulations of accretion onto a dipolar magnetosphere. I. Accretion curtains and the disk-locking paradigm. *A&A*, *508*, 1117-1133. doi: 10.1051/0004-6361/200912879